Technical Report
RAL-TR-1998-066

Contributions to EPAC - 98 by Members of the ISIS Facility

P Drumm (Editor)

1st December 1998

COUNCIL FOR THE CENTRAL LABORATORY OF THE RESEARCH COUNCILS

Enquiries about copyright, reproduction and requests for additional copies of this report should be addressed to:

The Central Laboratory of the Research Councils
Library and Information Services
Rutherford Appleton Laboratory
Chilton
Didcot
Oxfordshire
OX11 0QX
Tel: 01235 445384 Fax: 01235 446403
E-mail library@rl.ac.uk

ISSN 1358-6254

Contributions to

EPAC - 98

Sixth European Particle Accelerator Conference
22-26 June 1998
Stockholm City Conference Centre

by members of the ISIS Facility

D. Adams. C.P. Bailey. P.J.S.B. Barratt, J.R.J. Bennett, A.I. Borden, B. Brady, T.A. Broome,
M.A. Clarke-Gayther, I.S.K. Gardner, A.H. Kershaw, A. Letchford, R.D. Loyd,
G.R. Murdoch, C.W. Planner, C.R. Prior, A. Stevens, D.M. Wright
and U. Bessler*, A. Schempp*, H. Vormann*,

* members of I.A.P., Frankfurt, Germany.

Papers to be published in the Proceedings of EPAC-98.

August 1998
Paul Drumm, Editor

CONTENTS

† Oral presentation, ‡ Poster presentation

A REVIEW OF SPALLATION NEUTRON SOURCE ACCELERATORS

I.S.K. Gardner

Abstract

The operational performance of the current Spallation Neutron Sources and their possible upgrades are described. The new sources proposed, including the European Spallation Source, the Oak Ridge SNS and the Japanese proposals are reviewed. The differences in the designs of the accelerators and the methods used to control beam loss are highlighted.

1 INTRODUCTION

Accelerator driven pulsed spallation neutron sources have now been in operation for about two decades and are making significant contributions to forefront topics in neutron scattering science. Most of the sources have upgrade plans that will enhance their performance and some of the upgrades that involve accelerator developments are described.

The next generation of pulsed spallation neutron sources have significantly higher proton beam power and are now being researched, designed, and in some cases, funded. The proton beam powers of 10 - 200 kW achieved with the present sources will be increased to 0.5 - 5 MW in the new sources. In addition to the short pulsed sources, where the proton beam pulse length is about 1μs, long pulse sources with a pulse length of a few hundred micro-seconds are being considered and the CW source, SINQ at PSI, has started operation with a proton beam power of 1 MW at 590 MeV.

One of the most important factors in the design of all spallation neutron sources is the control of beam loss that may lead to activation of, or thermal damage to, the accelerator components. It is interesting to compare the beam loss control methods developed on the current generation of sources with the proposed methods for the new sources.

2 SOME EXISTING SOURCES AND THEIR UPGRADES

2.1 Existing Sources

Table 1 shows the main parameters of existing spallation sources.

2.2 Argonne National Laboratory, US. IPNS

IPNS operates with availability of over 95% for 25 weeks each year and has now been in operation for over 15 years. Although the beam power is only 7 kW the low PRF of 30 Hz, the Uranium Target enhancement factor of 2, and the use of solid methane moderators, provide a very competitive facility. An Enriched Uranium Booster Target has been used in the past to give a factor of 2 to 3 increase in neutron intensity. IPNS decided not to use another Booster Target due to the changes in operation required to deal with the increase in the delayed neutron

Table 1: The main parameters of some existing sources.

	IPNS Argonne USA	KENS KEK Japan	MLNSCE Los Alamos USA	ISIS RAL UK	SINQ PSI Switzerland
Accelerator	50 MeV Linac & Synchrotron	40 MeV Linac & Synchrotron	800 MeV Linac & Storage Ring	70 MeV Linac & Synchrotron	72 MeV Cyclotron & Cyclotron
p Energy (MeV)	450	500	800	800	590
Beam Current (μA)	15	4.6	70	200	1500
Repetition Rate (Hz)	30	20	20	50	Continuous
Beam Power (kW)	6.8	2.3	56	160	885
Injection System	H^- to p Foil	H^- to p Foil	H^- to H^0 Grad Mag H^0 to p Foil	H^- to p Foil	Direct p
Target Material	U^{238}	Tantalum	Tungsten	Tantalum	Zircaloy
No. of n Instruments	15	16	6	17	15
Last year's beam for n production (mA.hr)	63	4.5	144	672	~500

background and the requirements for dealing with enriched uranium.

An Enhancement Project will increase the productivity by improving the instruments, the accelerator, and the target/moderator/reflector systems. The proposed accelerator improvement will consist of the addition to the synchrotron of an rf system of twice the frequency of the present system. Although this project is not yet funded it is estimated that it will increase the proton beam intensity by 30-50%.

2.3 KEK National Laboratory, Japan. KENS

The KENS facility has been in operation since 1979 and has made a good improvement in beam intensity from 1.10^{12} to 2.10^{12} ppp over the last few years. The Booster Synchrotron produced 14.9 mA.hr of beam last year but the beam is shared with the 12 GeV Synchrotron, a Medical Facility and a Meson Laboratory leaving 4.5 mA.hrs for neutron production. Further work will cover non-intercepting beam profile monitors for the beam transport line, injection painting studies and development of a stripping foil with a single support edge. The main thrust is, however, now directed at the neutron source design for the JHF[1].

2.4 Los Alamos National Laboratory, US. MLNSCE

The MLNSCE Facility operated for 2060 hrs last year and produced 144 mA.hrs of beam. The facility is in the middle of a major improvement programme that is planned to take it to 200 μA beam current at 30 Hz, almost tripling the beam power, and making it one of the most powerful spallation sources available. This is coupled with an increase in the number of neutron scattering instruments from 6 to 14, and modifications of the Target/Moderator/Reflector systems for improved performance and greater ease of maintenance.

Great interest is shown in the performance of MLNSCE as it is based on an 800 MeV linac, capable of operation with a proton beam power of 1 MW, and a storage ring that employs H^- charge exchange injection, and this is the basis of design of several of the proposed, new Short Pulse Spallation Sources.

The present operation is limited to 70 μA beam current at 20 Hz by beam losses. Injection into the compressor ring uses 2 stage charge exchange with 1700 turns. H^- is stripped to H^0 via Stark effect in a high field magnet followed by H^0 to proton stripping in a carbon stripper foil. Studies have elucidated that the beam loss is attributable to "First Turn" losses (0.2 - 0.3 %) where excited H^0 states produced in the stripping foil strip to protons in the downstream dipole and are outside the acceptance of the ring, and to "Stored Beam" losses (0.3 - 0.5 %) from nuclear and large-angle Coulomb scattering produced as the protons in the stored beam pass repeatedly through the foil. The stripper magnet produces a factor of 3 emittance growth in the bend plane due to the statistical spread in the point where the stripping occurs, and this is followed by a large mismatch in the horizontal plane as the beam enters the ring. The H^0 beam, which enters the ring through a hole in one of the main dipoles, Figure 1, cannot be manipulated for painting the beam emittance into the ring.

A new injection scheme using direct H^- injection is being installed and will be commissioned during the summer of 1998, Figure 2. A merging dipole combines the incoming H^- beam with the circulating proton beam and the replacement of the ring window frame dipole downstream of the foil with two C-magnet dipoles allows improved handling of the "First Turn" losses. It is estimated that the stored beam foil hits will be reduced by a factor of 10 and that the overall loss rate will be reduced by a factor of 4 to 5 after optimisation of the foil thickness to reduce the excited H^0 states.

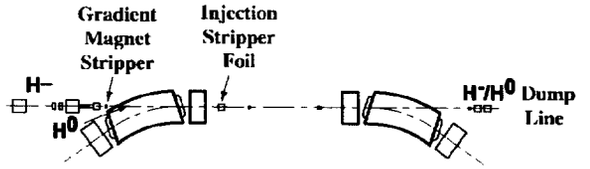

Figure 1. MLNSCE H^- to H^0 to p injection scheme

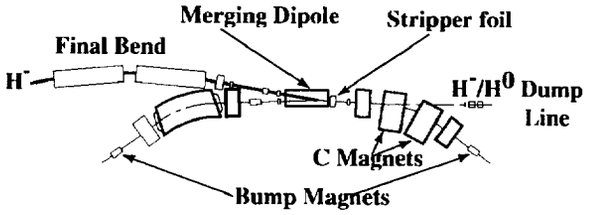

Figure 2. MLNSCE direct H^- injection scheme

A programme to double the Linac current, with a new H^- ion source, will allow shorter ring filling times and thus lower ring losses. This improvement will bring the PSR closer to its high intensity limit, set by sudden, substantial loss of the circulating beam. Interesting measurements show that the threshold for this effect can be altered by the amplitude of the ring rf, by the amount of beam in the gap between the beam bunches, and by the use of an inductive insert in the ring. The effect is thought to be due to an e-p instability, and while the effect will be studied further, it is expected that the introduction of a new ring rf system will allow 30 Hz operation at 200 μA.

Table 2: The main parameters of some proposed sources.

	SNS Oak Ridge USA	JHF KEK Japan	NSP JAERI Japan	ESS Europe	AUSTRON 11 Austria
Injector	1 GeV Linac	0.2 GeV Linac	1.5 GeV SC Linac	1.33 GeV Linac	130 MeV Linac
Ring	1 (2) Storage Rings	Synchrotron	1 (2) Storage Rings	2 Storage Rings	Synchrotron
p Energy (GeV)	1.0	3.0	1.5	1.334	1.6
Beam Current (mA)	1.0 (4.4)	0.2	1 (3.2)	3.7	0.13
Repetition Rate (Hz)	60	25	50	50	25
Beam Power (MW)	1.0 (4.4)	0.6	1.5 (5)	5	0.2
Linac I_{peak} (mA)	130	30	17 (30)	107	33
Linac Pulse (μs)	1000	<500	2000 (3720)	1200	187
Injection System	H^- to p Foil	H^- to p Foil	H^- to p Foil See text	H^- to p Foil	H^- to p Foil
No. Injected Turns per Ring	1200	250	1500 (2777)	1000	126

2.5 Rutherford Appleton Laboratory, UK. ISIS

The ISIS facility operates for 25 weeks a year and averages 90% availability for the accelerator and Target Moderator systems with a beam power of ~160 kW. The operating current is limited by the beam losses, but this limit is very close to the maximum intensity that can be achieved in the synchrotron at present. With the low injection energy of 70 MeV and direct H^- charge exchange injection, the losses associated with the injection process (~1%) are easily catered for with the H^0 and unstripped H^- beam picked up on a collector downstream of the 0.5 μm thick aluminium oxide foil. Up to 10% of the circulating injected beam is then lost in the trapping process and this beam is lost over the first 2.5 ms of the 10 ms acceleration period. The horizontal and vertical closed orbits of the synchrotron are minimised and adjusted to ensure that this lost beam is picked up on the 3 horizontal and 3 vertical, adjustable beam collectors, placed in the long straight section one superperiod downstream of the injection superperiod. A limit of 10 nA is set for the loss that occurs at the extraction septum magnet during beam extraction. Operation of the synchrotron can be limited by this loss. The rf trapping and the extraction loss are under study and this has highlighted the need for improved beam diagnostics for high intensity machines, to enable the behaviour of the small amounts of beam at the edges of the beam distributions to be studied.

Possible upgrades for ISIS include the addition of a second synchrotron rf system operating at twice the frequency of the present system and the addition of a second low frequency Target Station. Studies indicate that the new rf system will increase the beam current by up to 50% and the low frequency Target Station will enable increased neutron instrumentation specialising in the use of cold neutrons.

3 A COMPARISON OF PROPOSED SOURCES

3.1 General Design Considerations

Several new sources are under consideration and Table 2 lists some parameters of some of the proposed new sources. The high power spallation source designs include a linac and storage ring(s) as in ESS, ORNL SNS and JAERI NSP or a linac and synchrotron as in JHF and AUSTRON II. For the ESS a two synchrotron option was considered and would have been selected if the higher proton beam energy of 3 GeV had been needed for the target design. However, the synchrotron option was discarded because of its greater complexity and the higher space charge levels at low energies. The complexity is partly due to the large rf systems required and this was not considered to be offset by the benefits of less severe heat related problems for the H^- stripping foils and for the 50 Hz target.

The proton beam pulse length at the target must be of the order of 1μs to retain a sharp enough neutron pulse and this sets the total circumference of the synchrotron or compressor rings. Transverse stability criteria set the maximum circulating current in the rings. H^- charge exchange injection must be used for low enough losses from the necessary multi-turn injection process. The proton energy must be greater than 1 GeV to reach the plateau for neutron production per watt of beam power and to achieve acceptable energy density in the target. The loss mechanisms associated with the stripping foil, the peak foil temperature, and the need to move the circulating beam off the foil limit the number of injected turns to about 1000 per ring, thus setting the peak linac current required. This current is further increased by ~65% by the need to retain a gap in the circulating beam in the compressor rings for the rise time of the fast extraction kicker magnets. The gap is produced by a

beam chopper, at the ring rf frequency, in the low energy end of the linac. For the Oak Ridge SNS and the ESS this means peak linac H^- currents in excess of 100 mA. The achievement of such high currents, with low enough emittance to be transmitted through the linacs and with losses of less than 1 nA/m, infers the use of linac funnelling. The use of a funnel also allows twice the number of rf cycles to be filled with beam where the linac high energy section operates at a higher harmonic of the low energy sections.

3.2 Injection Schemes

The reference design for the ESS is described in [2]. Injection features simultaneous painting in all three phase planes of the two compressor rings to achieve low loss. A momentum ramp is produced by a cavity at the end of a 100m drift section following the linac. The beam then enters a 180° achromatic bend. The parameters of the drift section and the achromatic bend enable the beam to be scraped by stripping foils in the horizontal, vertical and momentum planes, ensuring that only beam of the specified parameters is delivered to the rings. The beam from the scrapers is taken to substantial, shielded beam dumps.

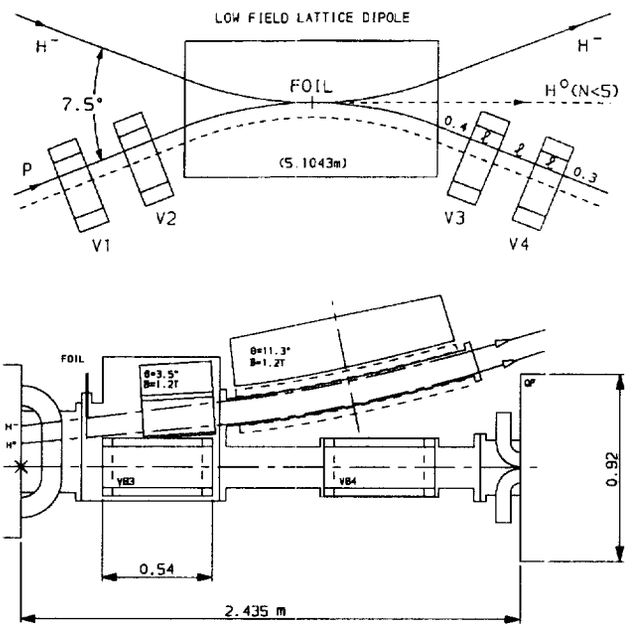

Figure 3. The ESS ring injection scheme.

Injection takes place in a low field bending magnet, Figure 3, to ensure that the unstripped H^- beam, and the H^0 beam and its excited states, are brought out of the ring to beam dumps or are accepted within the ring. Beam that is scattered by Coulomb interactions and nuclear interactions in the foil and the generated momentum tail is caught by downstream collectors [3]. A foil with two free edges is used and the circulating beam is moved progressively away from the foil by programmed currents in vertical orbit bump magnets and by changes to the frequency of the dual harmonic ring rf systems. Foil hits are estimated at less than seven per circulating proton, by the computations carried out allowing for full space charge effects [4]. However, foil temperature estimates are still seen to be near the limit and larger circumference rings are now being considered allowing the use of foil stripping or the new JAERI laser stripping mentioned below.

The Oak Ridge SNS is described in [5] and the injection scheme differs from that proposed for the ESS in that the H^- beam is merged with the circulating proton beam at a foil between a horizontal orbit bump magnet and a ring quadrupole. No momentum ramping is proposed and the pre-ring scraping is carried out in a 90° achromatic beam transport line. Figure 4 shows the layout of the low dispersion injection straight.

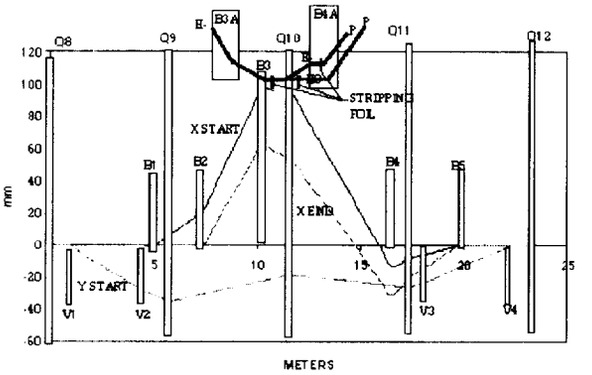

Figure 4. The Oak Ridge SNS ring injection scheme.

The JAERI NSP [6] considers foil stripping for the reference design but also studies a new concept of Laser stripping [7]. A section of an undulator magnet provides Stark stripping of the incoming H^- beam to H^0. The H^0 beam then drifts into the ring straight section where it is repeatedly excited to $H^0(3)$ by a laser and then stripped at the peak fields in a 7 period undulator magnet. It is estimated that each undulator half period will convert just under 50% of the H^0 beam present to $H^0(3)$ for high stripping efficiency. A pulsed laser of 1.5 kW power in conjunction with an optical resonator is assumed. The laser frequency and bandwidth must be matched to the energy and momentum spread of the incoming H^- beam.

A compressor ring lattice that includes both the JAERI Laser stripping scheme or the ESS foil stripping is being studied for the ESS, a section of which is shown in Figure 5.

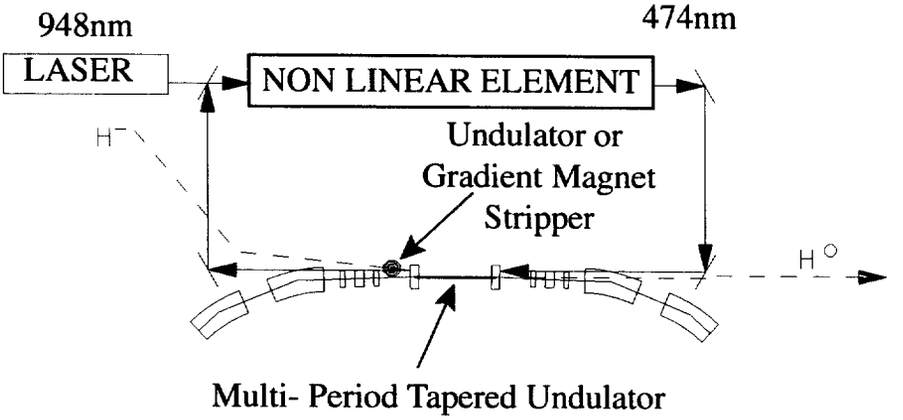

Figure 5. Elements of the JAERI Laser stripping scheme with Laser frequencies suited to ESS

Table 3. High current linac accelerating sections and frequencies

	RFQ		**DTL**		**CCDTL**	**CC Linac or Superconducting Linac**	
ORNL SNS	402.5		402.5	Funnel	805	805	MHz
APT US, France	350		350			700	MHz
JHF	324		324		-	972	MHz
ESSA	280		280	Funnel	560	560	MHz
ESS	175	Funnel	350		-	700	MHz
JAERI	200		200		-	600	MHz

3.3 Funnels and Choppers

Continuing studies on the ESS predict a 30 % emittance growth in the reference design beam chopper and angular dispersion in the funnel section. An alternative linac design (ESSA) is being considered and tests will also be made on a Funnelling RFQ at Frankfurt JWG University. The result of the studies and tests may be applicable to other high current linacs. The rf frequencies and linac accelerator sections for proposed high current linacs are shown in Table 3.

4 TIME SCALES

Of the new sources the ORNL SNS has the most clearly defined programme and is aiming for a phased approach that will deliver 1MW operation with one ring by 2006. The subsequent upgrades will take it to 4.4 MW with two rings.

The ESS has now entered a three year R&D phase which is a collaborative effort with several European Institutes. It is anticipated that this phase will be followed by a seven year construction period making the earliest operation at least ten years from now.

REFERENCES

[1] The JHF Accelerator Design Study Report. Sep 1997, KEK

[2] ESS. A next Generation Neutron Source for Europe. Vol. 3. The ESS Technical Study.
ISBN: 090 237 6 500 090 237 6 659

[3] C M Warsop, Beam Loss Collection on the ESS Accumulator Rings, EPAC98

[4] C R Prior, Longitudinal and Transverse Tracking Studies for ESS, AIP Conference Proceedings 377, 1995, p391

[5] The National Spallation Neutron Source Conceptual Design Report Documentation NSNS/CDR-5

[6] M Mizumoto, Neutron Science Project (NSP), JAERI

[7] Y Suzuki, A New Concept of Charge Exchange Injection for the High Intensity Proton Storage Ring of JAERI, APAC98

STATUS OF THE HIDIF STUDY

C.R. Prior

Abstract

The HIDIF study dating from 1994 explores the use of accelerated heavy ion beams as a driving mechanism for inertial confinement fusion. Representatives of several European laboratories, headed by the centre for heavy ion research, GSI, at Darmstadt, Germany, have collaborated to develop a self-consistent scheme based mainly on existing levels of technological expertise. The aim is to demonstrate the feasibility of an RF linac-compressor ring system for igniting an indirectly-driven deuterium-tritium target at a high repetition rate. The design is modular, which enables different aspects of the scheme to be investigated independently and provides the flexibility needed to respond to new ideas and future developments. Crucial issues include beam loss, the control of emittance and beam behaviour under current multiplication and space charge effects, while the need for further target development is becoming increasingly important. An overview of the study is presented and the status of research in the main aspects of the system discussed. Alternative ideas under consideration by the HIDIF group are also mentioned.

1 INTRODUCTION

With the declassification by the U.S.A. in 1994 of important material on target design, an opportunity was provided for re-consideration of heavy ion accelerators as drivers for inertial confinement fusion. Newly available data on indirectly driven targets prompted re-evaluation of earlier studies such as HIBALL [1], and a new design was prepared incorporating advances in accelerator technology and improvements in computational techniques. Up to 14 laboratories have been associated with the study, which at the end of 1997 culminated in a complete layout described in an interim report [2]. The ethos is for a power plant, utilising the special advantages provided by accelerator drivers in terms of efficiency, reliability and repetition rate, with the study aimed purely at demonstrating feasibility with no consideration of cost. Based on medium gain and short pulse duration, the design is modular in the sense that units may be multiplied as development advances into areas of higher driver energy and increased target gain

.2 THE HIDIF REFERENCE SCENARIO

Fig. 1 depicts the layout of the HIDIF reference design. The choice of driver energy of 3 MJ and target spot size of 1.7 mm derives from target gain curves published for the NIF project [3]. These figures determine to a large extent the layout of the driver, which adopts an RF linac-compressor ring approach, and set of parameters consistent with the requirements of the target-driver interface is given in Table 1.

Table 1: Main parameters of HIDIF reference design

Ion kinetic energy (GeV)	10
Total beam energy per pulse (MJ)	3
Linac peak current (mA)	400
No. of storage rings	12
No. of stored bunches	144
Stored bunch length (ns)	250
No. of ion species (telescoping)	3
Final pulse length (ns)	6
Peak power (TW)	750
Total peak current (kA)	75
Focal spot size (mm)	1.7
Number of final beam lines	48
Number of target convertors	2

The short pulse length and small focal spot size are the main problems to be faced in the design, together with requirements of low beam loss and minimum dilution of (6D) phase space in the rings. A technique known as "telescoping" is used, which avoids constraints of Liouville's theorem and involves three different ion species with masses differing by about 10%. These are accelerated to the same momentum within the same linac, but accumulated in different storage rings and taken on separate beam lines into different induction bunchers. During the final transport they are deflected into common beamlines and the differences in velocities (also ±10%) are used to bring all three ion species to the target at the same time. The central ion is taken to be singly charged bismuth ($^{209}Bi^{+}$), and rhenium ($^{186}Re^{+}$) and thorium ($^{232}Th^{+}$) are the other likely candidates.

2.1 Ion Sources

16 ion sources are used for each ion type and are designed for 35 mA of current with small beam emittances. Experiments at the University of Frankfurt with Bi^{+} have been carried out with plasma generators driven by arc discharge and a multi-aperture extraction system [2]. These have demonstrated feasibility and show good power efficiency, favourable for the cathode lifetime.

2.2 Linac Design

Initial acceleration through RF quadrupole linacs is followed by a four-stage funnelling system which

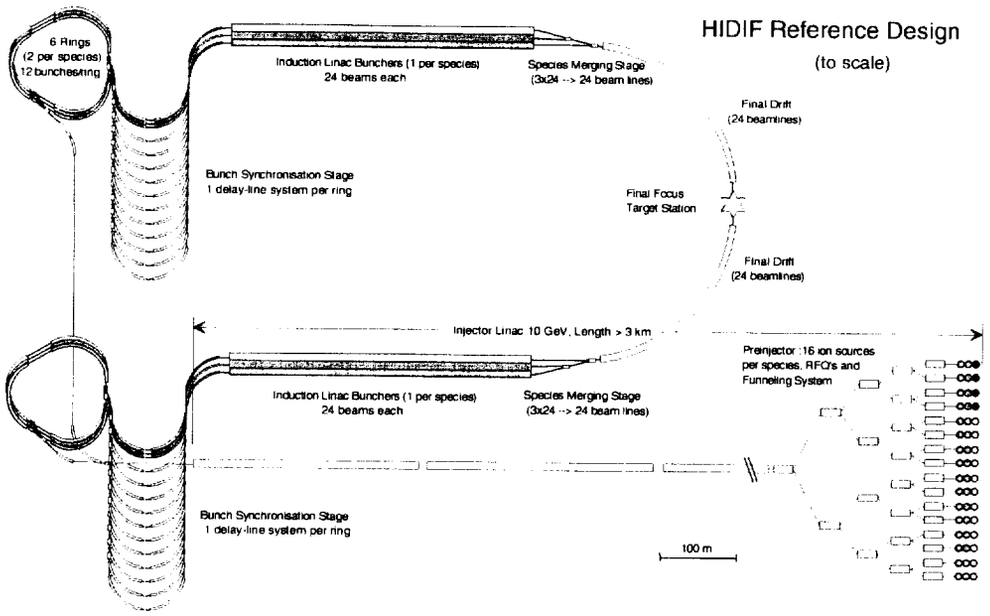

Figure 1: Layout of the HIDIF reference design

combines the pulses sequentially into the main linac. Parallel linac studies have been undertaken, the first for a conventional 200 MHz drift tube linac of the Alvarez type with a 5F5D focusing period [4]. This is designed to accelerate the ions to 10 GeV and a current of 400 mA, and meet ring injection requirements of (unnormalized, full) emittances of 4 (π) mm.mrad and a momentum spread, after bunch rotation, of $\pm$ 2.3 $\times$ 10^{-4}. The beam is also chopped into 250 ns macro-pulses for longitudinal injection into the ring. The second linac study is based on the use of H-mode cavities, which can handle high accelerating gradients. The use of multi-beam cavities in the low energy linac sections has also been suggested.

2.3. Compressor Rings; injection and extraction

The required total number of particles (~ 2 $\times$ 10^{15}) are accumulated in two stacks of six storage rings by multiturn injection and the current is multiplied by RF compression. Injection into the rings is via a tilted electrostatic septum, allowing simultaneous filling of both transverse phase planes. The choice of tunes is critical and, taking into account space charge, values of Q_h=8.57, Q_v=8.69 are found to be optimum when combined with programmed horizontal and vertical orbit bumps. Computer modelling suggests that 20 turns may be injected with beam losses of about 2% and final (99%) transverse emittances approximately equal to the 50 (π) mm.mrad of the reference design [5]. Analogous results have been found in a second study using a corner septum and slightly different combinations of tunes. Space charge tune shifts are only of the order of -0.04 and a conclusion from the analysis is that injection limitations stem more from losses through the mechanics of the process than from space charge effects. Longitudinally the linac macro-pulses are captured in RF barrier-like potential wells and compressed to about 120 ns. Simulations with the potential modelled by 5-7 Fourier harmonics based on h=12 as fundamental show nearly loss-free trapping and good longitudinal matching.

The storage ring itself has three superperiods, a mean radius of 70.474 m and uses long superconducting dipoles (6 T) in the arcs. Long dispersion-free straight sections provide flexibility for injection and extraction and space for the RF barrier bucket systems. Extraction is by fast kicker magnets with the extraction magnet superconducting. The choice of 12 bunches per storage ring is a consequence of estimates of the extraction kicker rise times.

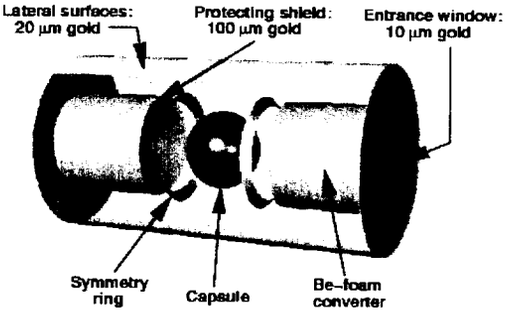

Figure 2: HIDIF Reference Target (Ramis 1997)

2.4 Transfer Lines and Final Focusing at Target

After current multiplication in the compressor rings, the bunches are transported via delay lines, one set per ring, with lengths differing in accordance with the bunch spacing, so that ions of each species arrive simultaneously at a set of induction linac bunchers. 24 bunches travel in a matrix arrangement side by side

through each of the bunchers, which are 440 m long and operate using a saw-toothed RF waveform to compress the bunches to 65 ns. Voltages of about 0.5 MV/m are required. A complicated scheme of quadrupoles and dipoles then merges one bunch of each ion species sequentially into a single line, timing the merging so that the different velocities of the species ultimately bring them into coincidence at the fusion target. During the final stages the bunches compress naturally to 6 ns.

Final focusing is based on conventional ballistic techniques using superconducting or pulsed quadrupoles. Separate beamlines are needed to reduce space charge effects, and in the HIDIF scenario twenty-four beams converge on the target from each side. These have first to be separated to create space for the quadrupoles. Each beamline carries a current of 1.2-1.5 kA, but studies show that, at this level, space charge is less of a problem than chromatic and other aberration effects in determining the fraction of the beam hitting the target converters.

An alternative approach under study is based on a plasma lens focusing the beam by the strong azimuthal magnetic field generated by a high current plasma discharge. The benefits are that the requirements of low emittance and energy spread may be relaxed and, since the beam would be largely space charge neutralised, the whole intensity could theoretically be transported in one focusing channel. The advantage for the reactor would be a lower number of beam ports, which would each have smaller area.

2.5 Target Design

Prompted by work on the NIF project, the target is assumed to be indirect-drive, using a hohlraum of a geometrical design to direct soft x-rays created by the impact of the heavy ions onto the target pellet. Earlier attempts at HIDIF designs were based around the "octopus" target of Basko [6] using eight convertors. However, a recent review suggested that x-ray conversion is only efficient (i.e. >50%) for very small spot sizes (<1 mm), which, because of emittance and other considerations, are difficult for an accelerator driver. For the 1.7 mm reference spot, x-ray conversion is less than 35%. Accordingly, the preferred model for HIDIF is now the target due to Ramis [7] shown in Fig. 2, a simpler, compact x-radiator with two-sided irradiation, with generally better coupling efficiency and offering the possibility of lower driver energy.

3 FURTHER DEVELOPMENT

The HIDIF group recognises that, notwithstanding the publication of an interim report [2], there is still much work to be carried out in fully optimising the beam-target coupling aspects of the design. Research into innovative target geometries, particularly those taking into account the properties of heavy ion beams, is needed and could lead to improved efficiency in the x-ray conversion.

Studies are being undertaken into the possibility of storing two beams of the same ion type but with different momenta in the same ring. The difference in particle velocities would be about 2%. Simulations show that compression in the barrier buckets is unchanged despite an overlap in the bunches of 0.5 μs.

Also under consideration is a model featuring ions with a higher charge state, since space charge appears to be less of a limiting factor in the rings than normal injection losses. Such a scheme would permit a shorter linac system and more efficient use of RF power. It may be that detailed evaluation of the consequences of beam losses during injection could lighten tolerances on some parameters and allow higher intensities in the rings. In addition, an alternative bunching scheme has recently been proposed [8] in which the present bunches are split into four sub-bunches with reduced momentum spread. The aim is to obviate the use of long induction linac bunchers, and investigation into the feasibility of the idea is currently in progress.

For any subsequent development to a full power driver, the HIDIF parameters would need to be scaled by a factor of at least three from their present basis of 3 MJ per pulse. This would place stringent demands on the linac high power RF generators, and require an extensive research and development programme from industry.

4 REFERENCES

[1] Badger *et al*, "HIBALL-II, An Improved Conceptual Heavy Ion Beam Driven Fusion Reactor Study", Karlsruhe Report KfK-3480, 1984.

[2] Plass and I. Hofmann (eds), "The HIDIF Study", to be published, 1998.

[3] Lindl, Nuovo Cimento, **106 A** 1467, 1993.

[4] Deitinghoff, G. Parisi, K. Bongardt and M. Pabst, "Error Effects and Parameter Analysis for a HIDIF DTL", Proceedings of this conference.

[5] Prior and G.H. Rees, "Multiturn Injection and Lattice Design for HIDIF", Proceedings of the 12th International Symposium on Heavy Ion Fusion, HIIF'97, Heidelberg, September 1997.

[6] Basko, "On Possible Target Designs for a 3,MJ Heavy Ion Ignition Facility", Proceedings of HIIF'97, *op. cit.*

[7] Ramis, "A 3 MJ Optimized Hohlraum Target for Heavy Ion Inertial Confinement Fusion", to be published in N.I.M.

[8] Schönauer, "An Alternative Scheme for Heavy Ion Driven Inertial Fusion", Proceedings of this conference.

A NEW HIGH DUTY FACTOR RFQ INJECTOR FOR ISIS†

H. Vormann*, A. Schempp*, U. Bessler*, C. W. Planner, A. Letchford

Abstract

The ISIS at RAL is going to be upgraded by a new injector. This injector will supply H--ions with beam currents up to 50 mA. It consists of a new ion source and a four-rod RFQ accelerator, designed for a duty factor as high as 10 %. In this paper the RFQ accelerator and the status of the project is being described.

1 INTRODUCTION

Rutherford Appleton Laboratory has a long-term experience in operating the ISIS neutron source [1]. Presently, the H^--Penning source is followed by a Cockroft-Walton injector and an Alvarez Drift Tube Linac. The ion beam is injected into the Synchrotron by charge change injection and finally sent to a heavy metal target.

The general data of the accelerator are the ion source extraction voltage of 35 kV, the injector output energy of 665 keV, the linac output energy of 70 MeV and the ISIS final energy of 800 MeV. In early 1997, a beam current of more than 55 mA has been reached with a stable operation at 2.5 % duty cycle. As the average beam current in regular operation is 0.2 mA, the average beam power at the target is as high as 160 kW. For the next generation neutron source, the European Spallation Source ESS, a duty cycle of 6.5 % is planned, with a beam power of 5 MW(1.34 GeV).

A new RFQ injector is being built for ISIS. The resonance frequency of the existing Alvarez Drift Tube Linac, and therefore of the new RFQ is 202.56 MHz It will be able to accelerate beam currents of 50 mA with high transmission. A later upgrade would allow beam currents up to 100 mA with 85 % transmission.

The main design feature of the new RFQ is the high duty cycle of 10 %, which is comparatively high for this kind of RF proton accelerators. Higher duty cycles have been used for heavy ion acceleration, e.g. at GSI for the HLI [2], but at lower frequencies.

The ISIS upgrade is a project which will improve the performance of ISIS and be helpful for the medium-term installation of ESS, because the injector can be tested under realistic conditions and later on be used for ESS. So it serves as a test bench for the future ESS injector.

The present plans for the European Spallation Source provide ESS project 107 mA beam current. This will be achieved with two RFQs, each accelerating 54 mA at 175 MHz, values, close to the parameters of the ISIS injector upgrade.

2 HIGH DUTY CYCLE RFQ

High Duty Factor accelerators have been used successfully for lower frequencies. At GSI Darmstadt, the Unilac HLI is working at 108.5 MHz at 25 % duty factor. Lower frequencies usually go along with larger resonators, therefore the power load is distributed on a larger surface. In the case of the four- rod- RFQ-structure most of the power is concentrated on the resonator insert, 33 % of the power is lost on the electrodes. Therefore, the electrodes are cooled by cooling tubes brazed to the back side of each electrode. Good experiences with this electrode cooling system have been made at GSI, the HLI-RFQ has been operated with an average power up to 15 kW/m.

A similar design will be used in the case of the H^--RFQ (202.56 MHz), where 40 % of the power is lost on the electrodes.

A short RFQ-resonator structure for high power operation (c.w.) has been built and tested. It worked well at c. w. at 20 kW/0.3 m, which corresponds to 60 kW/m, well above the required power for the ISIS upgrade [3].

E in	35 keV
E out	665 keV
ε^{in}_{norm}	1.00 π mm mrad
ε^{out}_{norm}	1.05 π mm mrad
ε^{out}_{norm}	1.15 π mm mrad
ε_{rms}	0.07 °MeV

Table 1: Beam parameters of the RFQ.

3 PARTICLE DYNAMICS

The particle dynamics design is based on the methods used for compact RFQs [4]. It uses adiabatic variation of parameters and rather high electrode voltage of 80 kV to have a high acceptance at a large aperture. The results have been tested with PARMTEQ simulations. Table 1 shows the beam dynamics parameters. Figure 1 shows results for simulations using the ideal two term potential.

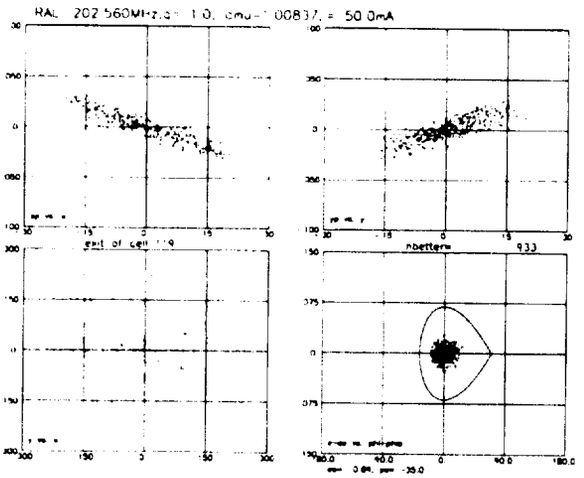

Figure 1. Particle output distribution.

A particle dynamics code which solves the field equations with respect to higher multipole components has been developed by Letchford [5]. These components appear due to the non-hyperbolic shape of the rod electrodes and the ratio of aperture to rod diameter chosen. The calculations showed that the design done for ideal quadrupoles needs only small modifications to match the properties of the hyperbolically shaped electrodes, respectively the geometric parameters have to be changed slightly to give the same beam dynamic results as for the ideal profile.

The multipole components can also be taken from MAFIA calculations, regarding the unavoidable multipole effects of the four rod structure with stems [6].

For achieving a good output emittance matching, the last cell of the accelerator has a special shape: it consists of half a RFQ-cell and one half cell with a symmetrical output matcher [7].

4. RF CALCULATIONS

Two requirements had to be combined in the new RFQ injector: High duty cycle and high electrode voltage, resulting in a very high average power load on the resonator.

MAFIA calculations have been done for optimizing the efficiency of the resonator and the field distribution.

One important topic was the increase of the resonance frequency with use of thicker stems, compared to earlier designs. The frequency of a resonator with standard stems is lower than 200 MHz. To reach the desired resonance frequency of 202.56 MHz, a set of tuning plates is mounted between the stems. With bigger stems the basic resonance frequency is somewhat higher than for RFQs for lower duty cycle.

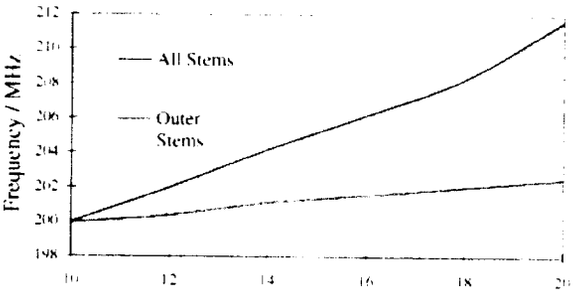

Figure 2: Resonance frequency vs stem thickness.

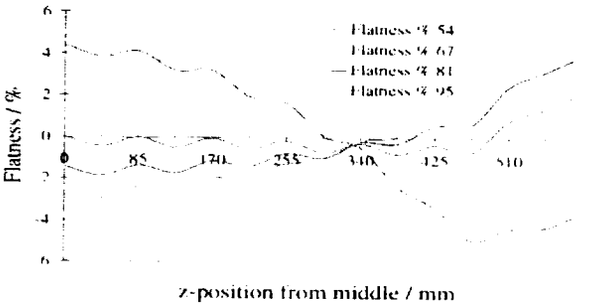

Figure 3. Flatness.

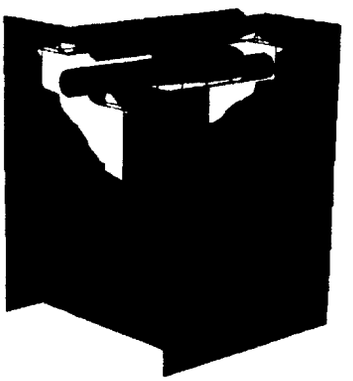

Figure 4: Power loss distribution in one resonator cell.

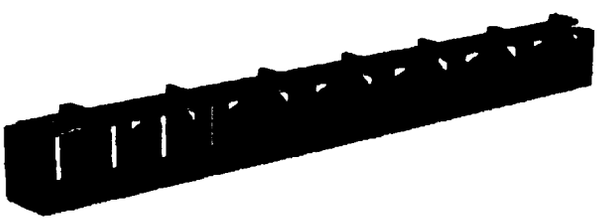

Figure 5: Mafia plot of the rf structure.

For reaching a good flatness along the beam line, various arrangements of tuning plates have been calculated with MAFIA. Figure 3 shows a plot of a field distribution for four tuning plate positions. The flatness percentage means the difference between the interelectrode voltage at the position z and the average intervene voltage ($f_z=(E-E_{av})/E_{av}$) along the beam axes. The parameters are the distance of the tuning plates,

placed in the structure, to the beam axis, in the first and the last resonator cell.

Figure 4 shows the power loss distribution in one cell, where brighter shades mean higher current densities and power loss per area. Figure 5 shows a Mafia plot of the resonator structure.

5 MECHANICAL DESIGN

For the layout of the cooling system indirect cooling by heat conduction in massive copper must be compared with cooling with a maximum number of cooling water tubes. It is important that the largest temperature difference for heat transport occurs at the transition from hot surfaces to flowing cooling fluids. Nevertheless, the effect of direct water cooling can only be exceeded if big solid copper parts are used. Cooling by massive copper parts can be comparable e.g. at the base plate of the RFQ insert.

For the ISIS RFQ a resonator without any water-to vacuum seals has been chosen. Where pipes have to be connected to massive copper stems inside the vacuum, they are brazed. The sealing of the cooling tubes against air is done with viton seals, sealing the stainless steel cooling pipes at the back of the resonance insert against the ground plate of the vacuum tank

The vacuum tank for the 4-Rod-RFQ has been slightly modified for high power operation to allow the pass-through of the 32 cooling pipes through the massive base plate.

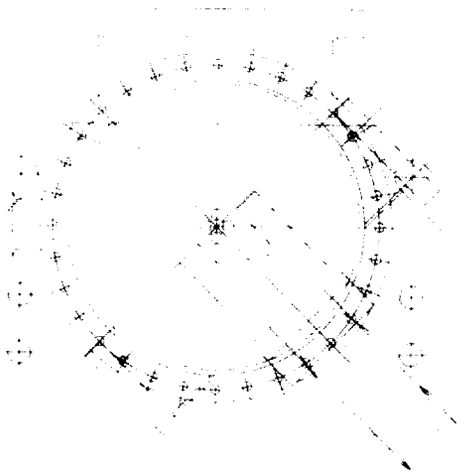

Figure 6: Cross section of the RFQ.

Calculations of heat transportation in the rf structure showed that a direct cooling of the ground plate is not necessary, as long as the stems are cooled. The temperature of the water will rise about less than 10^0C at the electrodes and the stems with a water flow of 3 l/min. The highest surface temperatures on the copper will be 55"C. Detailed calculations have been done by Murdoch[8] with a Finite Element Algorithm code. Experiments with models have been in good agreement with the simulations. Figure 7 shows a cross section of a directly cooled stem.

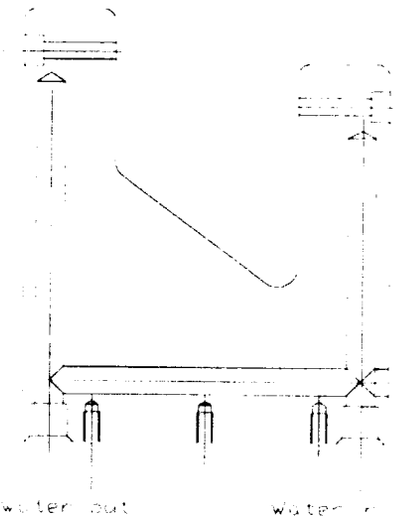

Figure 7: Cross section of a stem.

Table 2: RFQ specifications

Total Length	1190 mm
Diameter	250 mm
Frequency	202.56 MHz
Q-Value	3000
Shunt Impedance	65 kΩ

ACKNOWLEDGEMENTS

We would like to thank our colleagues from RAL for collaboration. We would also like to thank our group members for support and help, especially A. Firjahn-Andersch, A. Bechtold and F. Hoellering.

REFERENCES

[1] C. W. Planner et al, "High Stability Operation of the ISIS Pulsed Spallation Neutron Source at 200 μA", EPAC96, Sitges, Spain(1996), p584.
[2] J. Klabunde, E. Malwitz, J. Friedrich, A. Schempp, "Upgrade of the HLI-RFQ Accelerator", Linac94, KEK (1994), p704.
[3] A. Schempp, H. Vormann, "Design of a High Current H-RFQ Injector. PAC97, Vancouver.
[4] A. Schempp, "Design of compact RFQs", Linac96, CERN (1996), p53.
[5] A. Letchford, this conference.
[6] H. Vormann, A. Schempp, U.Beisel, O. Engels, T. Sieber, "The Design of RFQ Accelerators with High Duty Factors", EPAC96, Sitges, Spain (1996), p774.
[7] Ken Crandall, "Ending RFQ Vane Tips with quadrupole symmetry", Linac94, KEK(1994)p227.
[8] G. R. Murdoch, H. Vormann, this conference

† work supported by the BMBF

Thermal Design of an RFQ Cell for the Radio Frequency Quadrupole under construction for ISIS.

G.R. Murdoch, H. Vormann*

Abstract

A high duty cycle Radio Frequency Quadrupole (RFQ) accelerator is being designed and constructed under a collaboration between the Johann Wolfgang Goethe Universitat, Frankfurt, Germany and the CCLRC, Rutherford Appleton Laboratory, UK. This paper discusses the design of the cooling of an RFQ cell, the finite elements analysis of a thermal model under predicted heat load conditions and experiments to confirm the validity of the model.

1 INTRODUCTION

The RFQ has a design peak power of 200 kW operating at a 10% duty cycle, resulting in a surface heating of 20 kW distributed across 14 cells. Within each cell 34% appears on the electrodes, 44% on the electrode support stem and 22% on the rest of the cavity but mainly the ground plate [1].

To maintain the alignment and stability of an accelerated ion beam this heat must be dissipated to enable the RFQ to operate at a very stable temperature and limited thermal expansion.

The cells at each end of the vessel (numbers 1,2,13 & 14) have stems which are half the thickness of the rest and only one annular coaxial cooling channel. Potentially these are the most difficult to cool, hence they are taken as a worst case scenario. Cells 3 - 12 have stems with an inlet and outlet coaxial channel linked by a straight drilled channel. This configuration is shown in Figure 1 with the flow path identified.

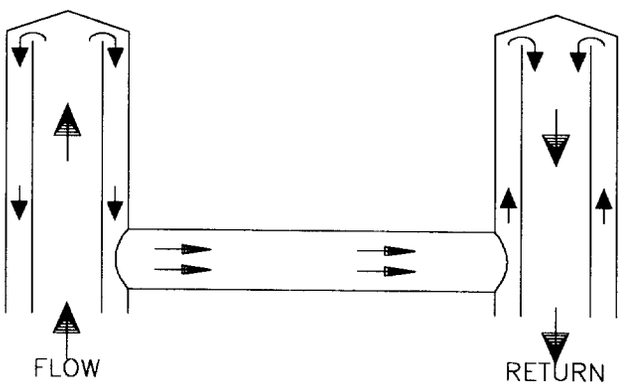

Figure 1.

The thermal finite element model yields a temperature profile for a specific cell, the nodal results file is then used to analyse the thermal expansion due to temperature gradients.

2 THERMAL CALCULATIONS

With a cooling water velocity, v, of 2.5 m/s in the coaxial inlet pipe an estimation of the pressure drop across a stem gives a value of ~0.8 bar. This suggests that each stem needs to be fed in parallel from a manifold in order to reduce the overall pressure drop across the RFQ vessel.

At this velocity the mass flow rate $m = 0.047\ kg/s$, (2.8 litres/min), the specific heat capacity of water c_p = 4200 J/kg K and with an expected heat load of 1.43 kW/cell the temperature rise across each cell is:

$$\Delta T = \frac{Q}{\dot{m} c_p} = \sim 7^\circ C$$

Calculating the heat transfer coefficient, h, for an annular coaxial channel is complex but an approximation can be obtained by substituting the equivalent diameter, d_e ,for the nominal diameter in expressions for the Reynolds and Prantl numbers [2].

The coaxial cooling channel has an equivalent diameter d_e= 0.002m, for a dynamic viscosity $\mu = 0.9 \times 10^{-3}$ kg/ms, density ρ = 1000kg/m^3 and a velocity of 4.6m/s in the annulus the Reynolds No. is:

$$\mathrm{Re} = \frac{\rho v d_e}{\mu} = 11231$$

For forced convection in a closed conduit the Nusselt number, Nu, is given by the modified Dittus-Boelter equation for turbulent flow:

$$Nu = 0.023\,\mathrm{Re}^{0.8}\,\mathrm{Pr}^{0.4} \qquad [2]$$

when $\mathrm{Re} \geq 10000$ & $0.7 \leq \mathrm{Pr} \leq 160$
with the thermal conductivity of water k = 0.6W/mK and the Prantl number being:

$$\mathrm{Pr} = \frac{c_p \mu}{k} = 6.3 \qquad \text{the} \qquad \mathrm{Nu} = 83.5$$

The heat transfer coefficient is given by:

$$h = \frac{Nu\,k}{d_e} = 25056 W/m^2 K = 0.025\, W/mm^2 K$$

The expected heat loss distribution on each cell gives heat load /unit area values of 0.0336, 0.0320 and 0.0324 W/mm^2 on the electrodes, stems and ground plate respectively. These values along with the heat transfer coefficient for the coaxial channel are used as the basic parameters to model an end cell with one coaxial cooling channel.

3 FINITE ELEMENT RESULTS

A 3-D ANSYS™ model of an end cell including its ground plate, stem and electrodes was analysed. Solid 87 elements which are 10-node tetrahedral in shape are used as they are ideally suited to meshing irregular shapes. Solid 92 are the equivalent structural element required for modelling the thermal expansion [3]. The meshing procedure is optimised by utilising element size and shape options. Applying the heat load and convection coefficient to the single coaxial channel model gives Figure 2.

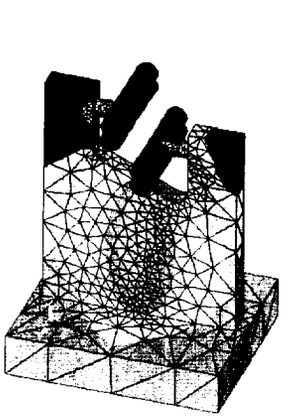

Figure 2.

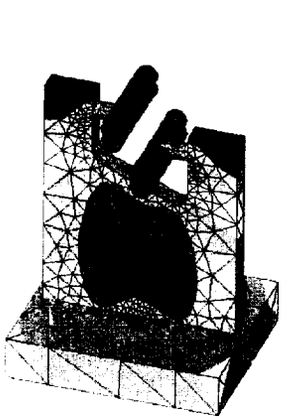

Figure 3.

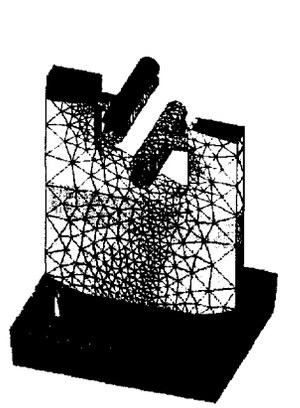

Figure 4.

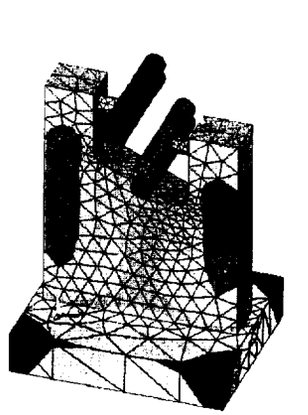

Figure 5.

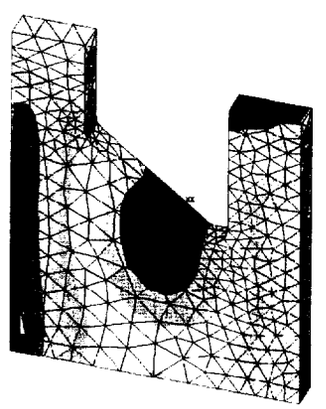

Figure 6.

A maximum temperature of 92°C is seen on the stem legs which support the electrodes. The ground plate temperature is around 86°C, but as the ground plate is rigidly bolted to the RFQ vessel any thermal expansion will be seen predominately on the stem. This

temperature gradient produces a maximum movement on the longer leg and is in the order of +0.2 mm in the 'Y' axis i.e. vertically upwards.
Running the RFQ with stems at such a high temperature presents many operational problems and is unacceptable.

Space for any modification to the cell design is limited because the cooling feed pipes for the electrodes run up through the ground plate via the stem legs, although, this may provide some level of cooling to the leg tips. However, there is sufficient space for the addition of another coaxial cooling channel inboard of the legs. Figure 3 shows the modified design with twin cooling channels. The maximum temperature is once again on the leg tips but has dropped to 68°C with the ground plate now being cooled more efficiently and seeing a temperature of 54 °C.

Analysing the same model structurally results in a maximum deflection in the 'Y' axis of 0.13 mm. This is shown in Figure 4.

Figure 5 shows a model of cells 3 - 12 which have a cooling channel design as shown in Figure 1. An overall maximum temperature of 47°C is seen on the ground plate with the leg tips reaching 40°C. This is lower than the twin channel end cell and consequently the thermal movement is less being in the order of +0.1mm.

4 EXPERIMENTAL TESTS & RESULTS

A full scale end cell stem is used as a test piece to verify the finite element model. A heater jacket applies a measured heat load to the test piece with 2.6 litres/min running through the cooling channel. Three type 'K' thermocouples are used to monitor temperature 10mm below the tips of the stem legs and mid-way along the slope between the stem legs. Two further thermocouples are used to monitor the input and output water temperatures. During tests the stem and jacket are wrapped in an insulating blanket to limit heat convection to air.

The stem was soaked for approximately 45 minutes with a total electrical input power of 770 W applied evenly to either side. The temperatures on the long stem leg, short stem leg and slope were 41.0, 44.1 and 43.7 respectively with the inlet and outlet temperatures being 27.3 and 31.4°C. This temperature rise equates to 746 W of heat being dissipated to the cooling water.

A finite element model is used to simulate the exact conditions of the test. Applying the same heat load to the finite element model and using revised heat transfer coefficients with a staggered bulk fluid temperature produces Figure 6. There is good correlation between the experimental results and finite element model with the long stem leg, short stem leg and slope showing temperatures of ~46, 48 and 50°C respectively i.e. within 12% of the experimental values.

5 CONCLUSIONS

The addition of another coaxial cooling channel in the end cells drops the maximum temperature of the stems to a more acceptable operational level. This temperature drop, by definition, decreases any movement of the electrodes resulting in a more stable RFQ structure. Movement of cells 3 -12 is smaller but if development tests highlight problems with uneven thermal expansions then the flow to these cells may be adjusted so that all cell movements are the same.

The experimental results show that the finite element model is sound albeit slightly pessimistic and gives confidence in its use during further developments.

REFERENCES

[1] Hartmut Vormann, Johann Wolfgang Goethe Universitat, Private Communication.
[2] William S Janna , Engineering Heat Transfer, SI Edition, Chapter 11.
[3] ANSYS™ Elements User's Manual Revision 5.0, Volume 3.

Limits in the design of short solenoids for use in matching into RFQs

C.P.Bailey

Abstract

An examination of the limits of solenoid length to bore ratio for a practical solenoid design is described, with reference to the linear matrix representation. Tracking of a four dimensional particle distribution through a finite element model of a solenoid design is compared with the matrix transform of the phase space ellipses describing the distribution. A design is presented based on these results for the solenoid matching system between the ion source and RFQ for the new ISIS preinjector.

1 INTRODUCTION

The ISIS ion source is an asymmetric slit source and as shown by Planner[1], three or four solenoids are required to match the ion source to the RFQ. There is a restriction on space available for the solenoids on ISIS, and this paper describes the calculations carried out to optimise the design of solenoids within the available space, particularly for determining the minimum acceptable length/bore ratio which is here shown to be ~3.0 - 3.5.

2 PARTICLE TRACKING THROUGH SOLENOIDS

The solenoids have been modelled with Vector Fields Opera2d, Opera3d and Tosca software. Particle tracking through single magnets and through matching systems was initially done in Opera2d. However to model the effects of tolerances in the manufacture of the solenoids it was necessary to model them in 3d.

In order to be able to track a large number of particles through the solenoids without spending excessive time, the magnetic fields computed by the Vector Fields software were represented by coarser meshes of points, and the particles were tracked through these coarser meshes. The magnetic system was assumed to be linear so that changes to the overall magnetic field strength were accommodated simply by linear scaling.

This procedure made it possible to model distributions containing many thousands of particles and hence produce a clearer picture of the aberrations generated in the system. Once the model of the required magnets has been produced it also makes it very simple to change the separation between magnets or the field strength in them.

The models of the magnets are calculated with the field level set just below the level at which the case material begins to saturate, in the models here using 6 Amm^{-2} in the drive coils. This avoids any distortions in the fields caused by the saturation. However it does mean that saturation is not accounted for if the field is scaled to a higher level. Also the tracking currently does not include any space charge effects.

Checks on the calculations were made by carrying out complementary calculations based on the linear matrix representation of Larsen[2]. In this representation the solenoid is represented by a uniform field extending over the effective length together with 'delta function' end effects, and the particle distributions are represented by the usual elliptical boundaries. Comparisons between the finite element method and matrix method can be made anywhere except within the effective ends of the solenoids.

The effective length, of each magnet, is calculated by comparing the matrix ellipses and the tracked distribution. The ellipses are calculated for a test field level with an estimated effective length. The nominal level of the field distribution is set to a value such that the $\int Bdl$ over the estimated effective length is the same as that calculated along the axis of the finite element model. The length at which the highest fraction of tracked particles falls within both ellipses is used as the effective length.

The Trace computer code is used with this length to calculate the required field levels for the matching system. The beam is tracked through the whole system and the final distribution plotted to show any deviations from linear matrix match.

3 MAGNET DESIGN

The design of the solenoids uses an increased bore through the central part of the coils, based on a CERN design described in [3]. This improves the flatness of the field in the centre of the magnet and enhances the sharpness of the end fields, both of which reduce aberrations. The model also includes the clearance between the outside of the coils and the casing which is

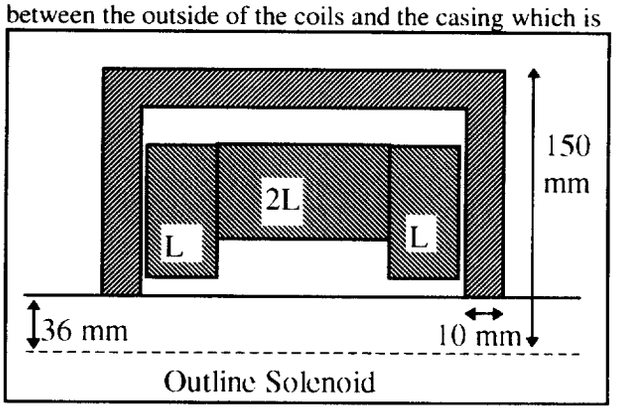

required to accommodate the connections to the coils, but not the current in these connections nor the holes through the casing.

The coils, but not the case, are also slightly withdrawn from the beam pipe which puts the edges of the field outside the beam pipe. This is produces a slightly more uniform field than using the whole of a smaller bore

4 RESULTS

Finite element models have been run for solenoids ranging in length between 90 and 300 mm, all with a 72 mm bore and 10 mm thick end walls. An identical input beam is tracked through each solenoid.

The table below shows nominal field in each magnet, the variation in effective length/ mechanical length, and a qualitative description of the aberration after a single solenoid. The pictures opposite show the beam after a system of 3 solenoids, which in the matrix case enables a common match to be achieved, and shows the increase in aberration much more clearly than through a single magnet.

length	length / bore	B nom	eff. length /mech. length	aberration
90	1.25	.277	1.200	Very strong
120	1.67	.310	1.117	significant
150	2.08	.343	1.067	visible
180	2.50	.364	1.039	just
210	2.92	.383	1.019	just
240	3.33	.388	1.008	no
270	3.75	.396	1.011	no
300	4.17	.398	1.010	no

The plot shows the effective length/ mechanical length and the nominal field, as a function of length / bore..

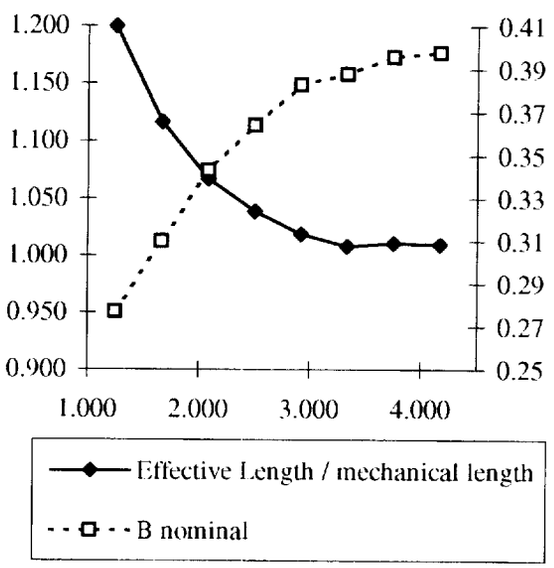

In all cases at the effective length, after a single

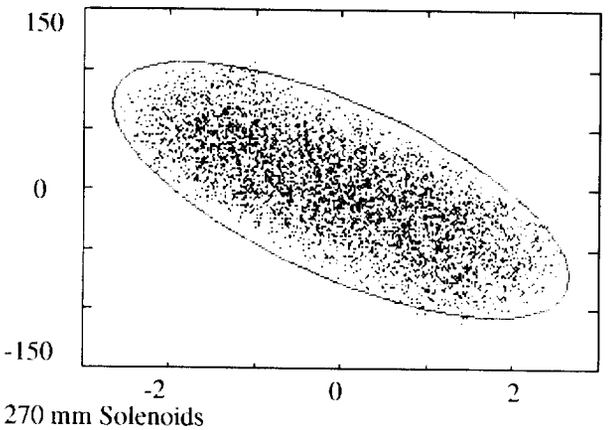

270 mm Solenoids

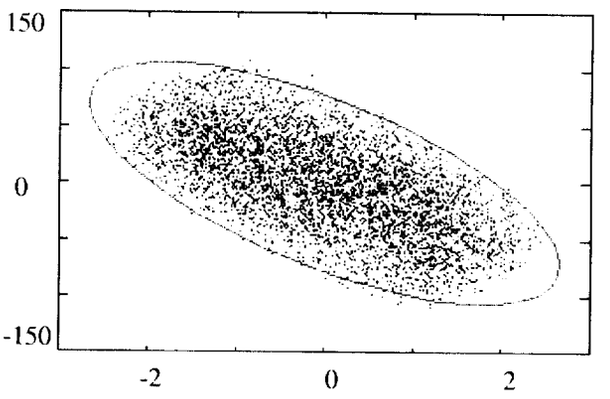

210 mm Solenoids

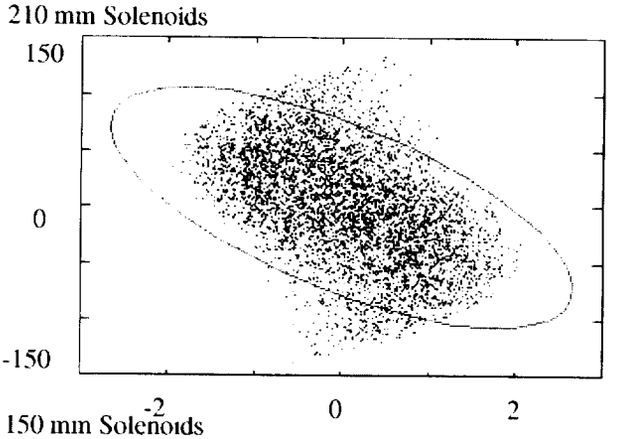

150 mm Solenoids

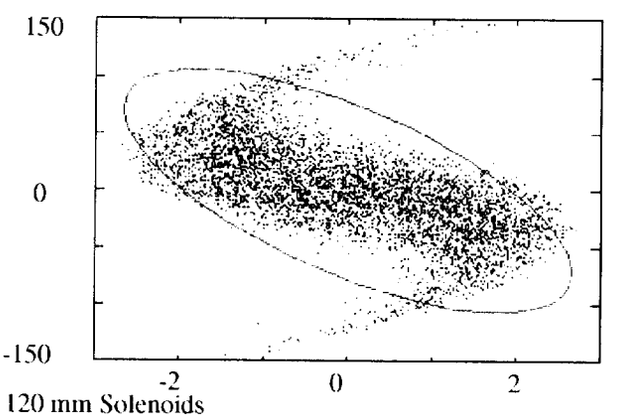

120 mm Solenoids

Increase in aberration through matching system with decreasing length of solenoid. x x' plot. Ellipse α=0.92 β=0.034 ε=208

magnet over 95% of the particles are contained within the ellipses. This rises to 98% or more at length to bore ratios over 3. There is also visible S bending in the distributions up to 3 and some distortion from an ellipse just beyond. The plots of effective length / mechanical length and nominal field against length to bore, show turning points at around 3.5.

These effects all occurring in the same region suggest that 3.0-3.5 is a sensible limit to the minimum length to bore ratio of a low aberration solenoid.

5 THE DESIGN FOR ISIS

The existing ISIS ion source is used with a single gap post accelerator to bring the beam energy to 35 keV. The system was initially designed using two solenoids with a length to bore ratio of 4 and due to the constrained length one low power solenoid with a length to bore ratio of 2.5. The first solenoid is mounted close to the ground electrode of the accelerating gap, and abuts the second low power solenoid. This gives the longest possible, gap to accommodate the required diagnostics, before the final solenoid which has to be positioned as close to the RFQ as possible.

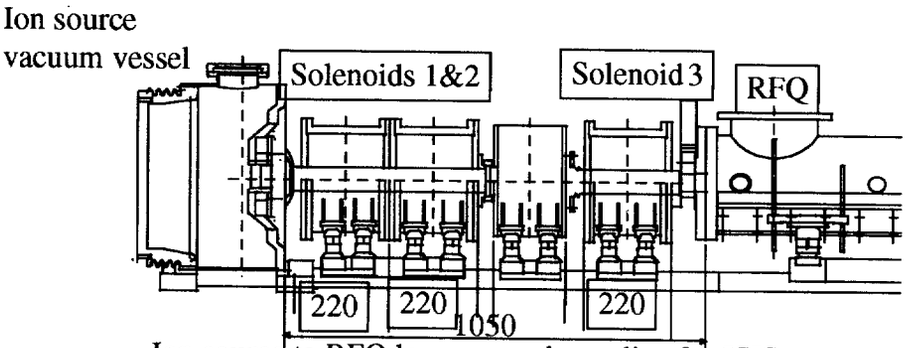

Ion source to RFQ low energy beam line for ISIS

The system is tightly length constrained to replace the existing LEDS equipment in the ISIS injector without preventing their reinstallation. However to gain the advantage of only designing and manufacturing a single type of magnet it was decided to make all three the same. This required the longer magnets to be shortened slightly, and together with an increase in the bore has reduced the ratio to 3. The net effect on the system aberrations is slightly beneficial.

The magnet design chosen differs from those modelled and presented here in that it has thicker end walls, which further reduce any effects of saturation in the casing. As a result the effective length is shorter than physical length.

The magnet and system designs have been checked using Trace2d including residual space charge up to 30 mA and using 3d tracking with zero space charge.

REFERENCES

[1] Matching unequal transverse emittances from an H- ion source into an RFQ. C.W.Planner Particle accelerators vol48 1995.

[2] Transport Matrices for a Magnetic solenoid. R.Larsen, Spear 107, 1971.

[3] Study of LEBT for RFQ2 G.Rossat, M.Weiss, PS/LI/note 85-1 , CERN 1985

A comparison of 4-rod and 4-vane RFQ fields.

A. Letchford and A. Schempp*

Abstract

A 202.5 MHz, 665 keV, H 4-rod Radio Frequency Quadrupole, designed by the Institüt für Angewandt Physik at Frankfurt University, will replace the existing DC pre-injector on the ISIS Spallation Neutron Source at R.A.L. The 4-rod RFQ offers some advantages over 4-vane designs in terms of RF properties and ease of manufacture. However, the rod shaped electrodes give cells where the pole tips have constant centre of curvature rather than the constant transverse radius of curvature which is usual for pole tips of vane electrodes. In order to investigate the effects of this difference in geometry, new codes have been written to calculate a multipole expansion of the RFQ potential and simulate the beam dynamics in the resulting field. Results are presented comparing similar 4-rod and 4-vane designs. For the 4-vane design a comparison is made with the Los Alamos code PARMTEQM [1].

1 RFQ POTENTIAL

Following the method of Kapchinski and Tepliakov (KT)[1] it is possible to derive an expression for the potential between the electrodes of a single RFQ cell [2]:

Where m+n = 2p+1. V is the potential difference between two electrodes, $k = \pi/L$ and L is the length of the cell. I_{2n} is the modified bessel function of order 2n

$$U(r,\theta,z) = \frac{V}{2}\sum_{p} A_{0(2p+1)} r^{2(2p+1)} \cos[2(2p+1)\theta] + \frac{V}{2}\sum_{n}\sum_{m} A_{mn} I_{2n}(mkr)\cos(2n\theta)\cos(mkz) \qquad (1)$$

and the A_{xx} are the multipole coefficients whose values depend on the pole tip geometry.

1.1 Two Term Potential

In order to approach RFQ design analytically, only the first term in each series of equation (1) is taken. This results in the two term potential function (TTF):

(2)

Given a cell with aperture 'a' and modulation 'm' then analytical expressions exist for A_{01} and A_{10}. A_{10} is often

$$U(r,\theta,z) = \frac{V}{2}\left[A_{01} r^2 \cos(2\theta) + A_{10} I_0(kr)\cos(kz)\right]$$

abbreviated to A and is called the acceleration efficiency. Another useful definition is the focusing force factor B:

Design recipes from KT and others [1][3] allow values of A and B to be calculated for the desired beam dynamics in the RFQ.

2 POLE TIP GEOMETRY

$$B = \frac{q}{m_0 c^2}\lambda^2 A_{01} V \qquad (3)$$

Equation (2) describes equipotential surfaces with hyperbolic transverse sections. To generate the pure two term potential, electrodes would be required with this same hyperbolic shape. In practice, due to limits on the peak surface electric field and also to allow for ease of manufacture, the geometry of the electrode pole tip deviates from this ideal, often having a circular section. The two types of pole tip in common use are the vane type and the rod type as illustrated in Figure 1.

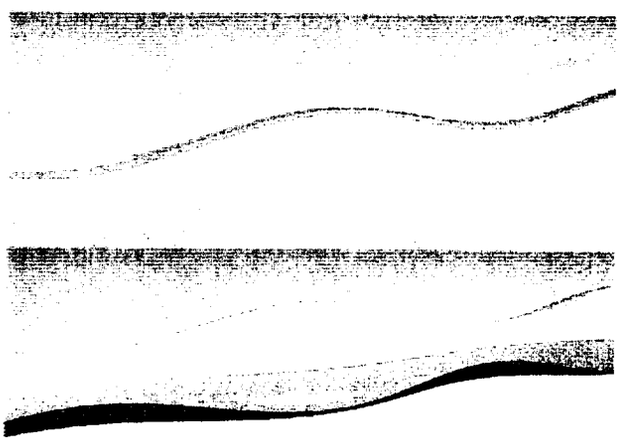

Figure 1: Approx. two periods of pole tip for a vane electrode (top) and a rod electrode (bottom).

The tip of the vane has the same transverse radius along the cell. By contrast, the rod's radius is a function of longitudinal position and modulation. The TTF is a poor approximation to these real electrode shapes so in order to more accurately calculate the resulting field additional terms are required in the potential function.

3 EIGHT TERM POTENTIAL

A program, RFQSIM, has been written to calculate the coefficients of a potential function using the eight lowest order terms of equation (1):

[1] 'PARMTEQM' refers to the LANL RFQ design codes RFQUICK, PARI & PARMTEQM.

$$U(r,\theta,z) = A_{11} r^2 \cos(2\theta) + A_{03} r^6 \cos(6\theta) + \quad (4)$$
$$A_{10} I_0(kr)\cos(kz) + A_{12} I_4(kr)\cos(4\theta)\cos(kz) +$$
$$A_{21} I_2(2kr)\cos(2\theta)\cos(2kz) + A_{30} I_0(3kr)\cos(3kz) +$$
$$A_{23} I_6(2kr)\cos(6\theta)\cos(2kz) + A_{12} I_4(3kr)\cos(4\theta)\cos(3kz)$$

RFQSIM can in principle calculate the coefficients for any geometry for which the boundary can be defined. So far only constant radius vanes and rods have been investigated.

3.1 Calculation of coefficients

The coefficients are calculated by a least mean squared (LMS) error fit to the boundary defined by the known electrode surface. For each point on the surface, U, r, θ and z are known in equation (4) giving an expression with the coefficients as unknowns. The LMS fit is performed using 10000 surface points for each cell: 100 around the pole tip for each of 100 longitudinal positions. This is a fast method of calculating the coefficients as it doesn't rely on solutions found by over-relaxation. It is also flexible because there are no look-up tables for pre-defined geometries.

3.2 Adjustment of cell parameters.

Given design values of A & B the problem is to find a cell geometry that achieves these values. Starting with values of a & m from the TTF, RFQSIM iteratively adjusts the cell parameters until A & B are within 1% of the design values. For vane electrodes the quantity ρ_0/r_0 is held at the design value as the cell is adjusted. For rods the quantity ρ_0+r_0 is preserved. r_0 is the mid-cell aperture and ρ_0 is the mid-cell transverse radius.

4 RESULTS

RFQSIM does time dependant tracking of macro-particles through the calculated field. A 3D, PPI space charge algorithm is used and multiple bunches are tracked. The results presented are for the ISIS RFQ design of Schempp[4] with ρ_0/r_0 = 0.83. Four 'designs' have been investigated.

Design 1: Coefficient calculation and tracking by PARMTEQM. Vane electrodes.

Design 2: Coefficient calculation by PARMTEQM. Tracking by RFQSIM. Vane electrodes.

Design 3: Coefficient calculation and tracking by RFQSIM. Vane electrodes.

Design 4: Coefficient calculation and tracking by RFQSIM. Rod electrodes.

Table 1 gives the transmission efficiency and final energy for each design with a beam current of 20 mA. Only accelerated beam is included.

Table 1: Transmission efficiency and final energy

Design	Transmission	Final Energy
1	92.7 %	665 keV
2	94.6 %	665 keV
3	89.9 %	665 keV
4	96.8 %	664 keV

When using the same coefficients (Designs 1 & 2), RFQSIM and PARMTEQM are in close agreement. The difference in transmission of ~2% can easily be explained by the different space charge algorithms and different criteria for lost particles. Figure 2 shows the output phase space distributions.

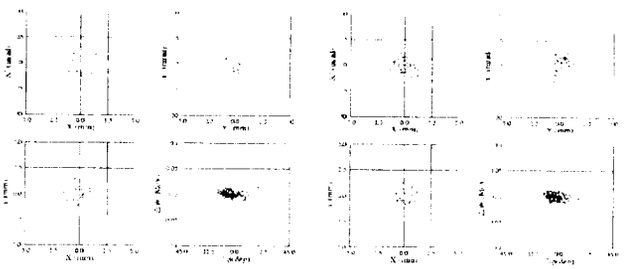

Figure 2: Output phase space distributions. Left - Design 1, Right - Design 2.

There is clearly quite good qualitative agreement between the two codes. As PARMTEQM is considered the 'industry standard' code this is a useful test of the beam dynamics part of RFQSIM.

When RFQSIM calculates the coefficients for vane electrodes (Design 3), the resulting design has a transmission ~5% less than the PARMTEQM design (2). Examination of the coefficients shows that Design 3 has a slightly lower value of B in the early cells of the RFQ as shown in Figure 3.

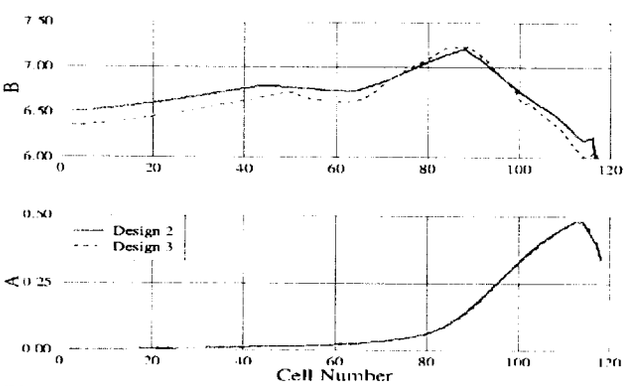

Figure 3: Values of A & B for Designs 2 & 3.

This slightly reduced focusing results in a larger beam radius in later cells and accounts for some of the additional beam loss. As the values of B in Design 3 are very close to the design values this implies that the PARMTEQM coefficients give a value of B which is slightly too high in the early cells. Also, in later cells

where the modulation is larger, RFQSIM calculates larger high order terms in the potential as can be seen from Figure 4. This may also account for additional loss.

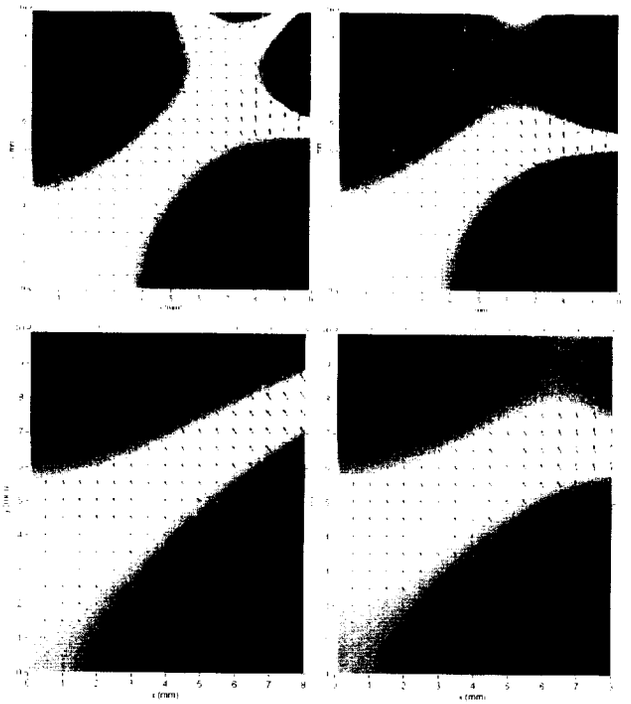

Figure 4: Electric potential and field in cell 40 (top) and cell 114 (bottom) for Design 2 (left) and Design 3 (right).

In Figure 4 the black regions are the electrodes ($U \geq 1$) and the colours represent the potential from U=+1 (red) to U=-1 (blue). The plots are made at z=0, the entrance plane of the cell. The spurious 'electrode' in the top plots results from the truncated series of equation (4). In cell 40 where the modulation is modest, the potential plots are very similar. In cell 114 where the modulation is greater, the PARMTEQM coefficients give electrodes which are closer to the hyperbolic shape of the TTF. That these are vane electrodes can be seen from the plot at lower right where the pole tips have equal radius.

4.1 Comparison with rods

Table 1 shows that Design 4, with rod electrodes, gives the highest transmission. This design has almost identical values of A and B to Design 3. One might expect that the more complex geometry of the rods would result in a potential with larger high order terms which in turn might be detrimental to performance. In practice however, this effect is balanced by more favourable cell parameters as shown in Figure 5. The aperture is increased by as much as 5% and the modulation is considerably decreased in the final cells.

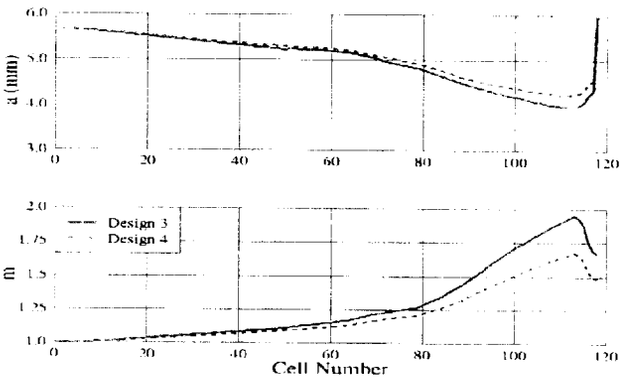

Figure 5: Values of a & m for Designs 3 & 4.

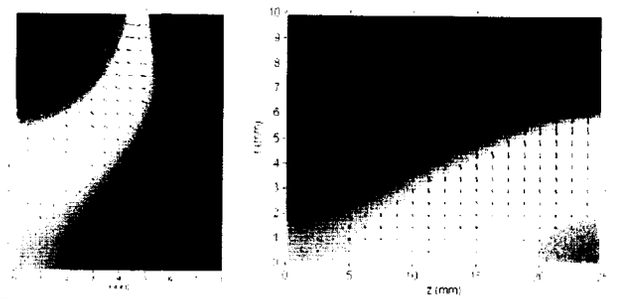

Figure 6: Electric potential and field in cell 114 of Design 4. Left - transverse, Right - longitudinal.

Figure 6 shows examples of the potential in Design 4. The longitudinal plot is at θ=0 and shows the horizontal electrode. It is clear from the transverse plot that the eight term potential is struggling to approximate the electrode shape away from the beam axis although the effect in the beam region appears to be small. It can be seen that the two pole tips have the same centre of curvature which is correct for rod electrodes.

5 CONCLUSIONS

For 4 vane designs, RFQSIM has performance comparable to PARMTEQM. For 4 rod RFQs, these results suggest that the same beam dynamical design can be achieved with a larger aperture and smaller modulation compared to the equivalent 4 vane RFQ. Code validation will form an important part of the ISIS RFQ test programme.

REFERENCES

[1] I. M. Kapchinski and V. A. Tepliakov, "Linear Ion Accelerator with Spatially Homogenous Strong Focusing", Prib. Tekh. Eksp., No 2, 19, 1970.

[2] C. Biscari, "Computer Programs and Methods for the Design of High Intensity RFQs", CERN/PS 85-67 (L1), CERN, 1985.

[3] K. R. Crandall, R. H. Stokes and T. P. Wangler, "RF Quadrupole Beam Dynamics Design Studies", Proceedings of the LINAC conference, Montauk, NY, 1979.

[4] U. Bessler, A. Schempp, H. Vormann, A.Letchford, "A New High Duty Factor RFQ Injector for ISIS", these proceedings.

A COMBINED FUNCTION BEAM EMITTANCE AND PROFILE MEASURING SYSTEM FOR THE ISIS 665 keV H⁻ PRE-INJECTOR

Michael A. Clarke-Gayther

Abstract

A description is given of the combined function, beam emittance and profile measuring system, installed on the 665 keV H– pre-injector at ISIS, the high intensity pulsed neutron source at the Rutherford Appleton Laboratory. The computer controlled system, consisting of in-vacuum beam analysing slits, and multiwire detectors, linear actuators, position encoders, motor drives, and signal conditioning electronics, measures the transverse emittance and profile of the 300 μs, 35 mA, 665 keV H– beam, with high precision.

1 INTRODUCTION

The concept and accurate measurement of beam emittance are of fundamental importance to the design and operation of particle accelerators. This description of the beam, when combined with a knowledge of those forces and processes that act on the beam (e.g. acceleration, space charge, scattering), enables the accurate prediction, and modelling of beam dynamics to be made, in accelerators and transport beamlines.

A particle beam, consisting of an ensemble of particles, each defined in terms of a total energy function, or Hamiltonian (H), is characterised by defining beam emittance, as the volume of a hyper-ellipsoid in six dimensional phase space, with the canonical coordinates x, p_x, y, p_y, z, p_z [1].

In practise, emittance is measured at constant beam energy, and by techniques that evaluate the 'root mean square' (rms) density distribution in the six dimensional phase space, in terms of elliptical area projections in the two dimensional longitudinal sub-space, with phase and energy coordinates (φ, *W*) , and the four dimensional transverse sub-space, with position and divergence coordinates (x, x', y, y') or (r, r').

Measurement systems, fall into two distinct groups, those for the determination of longitudinal emittance ($\Delta\varphi/\varphi$, $\Delta p_z/p_z$) [2], and those for the determination of transverse emittance (x, x', y, y') or (r, r') [3]. Systems can be non-destructive or destructive to the beam. The former include the wire-shadow and tomographic methods [3], both capable of being implemented in H- beams using the laser detachment method [4]. The latter systems include the pepper pot, electric sweep, slit-slit, and slit-harp [3]. A computer controlled, slit-harp emittance, and profile measurement system has been installed on the 665 keV H- pre-injector at ISIS.

2 EMITTANCE MEASUREMENT

The transverse beam emittance ε is defined as the volume of a four dimensional hyper-ellipsoid given by :

$$\varepsilon_{x,y} = \frac{1}{\pi}\int\int\int\int dx\,dx'\,dy\,dy'$$

The measurement evaluates $\varepsilon_{x,y}$ in terms of the two dimensional projections in the x, x' , and y, y' planes :

$$\varepsilon_x = \frac{1}{\pi}\int dx\,dx' = \frac{1}{\pi}\cdot A_x\ ,\quad \varepsilon_y = \frac{1}{\pi}\int dy\,dy' = \frac{1}{\pi}\cdot A_y$$

where A_x and A_y are elliptical areas in the x, x' , and y, y' planes, for 'normal', or 'perfect' beams [1]. For real beams, the evaluation of rms emittance, defines the ellipse area, of a transportable 'equivalent perfect beam', that is an invariant of motion in linear focusing transport systems [1]. This area is defined in terms of the second order moments, $\overline{y^2}$, $\overline{y'^2}$, $\overline{y\cdot y'}$, of the density distribution $\rho_2(y, y')$ as : $\varepsilon_{rms} = \sqrt{\overline{y^2}\cdot\overline{y'^2} - (\overline{y\cdot y'})^2}$

Evaluation of ε_{rms}, and the related Twiss parameters, at one point in a beam transport system, enables an accurate prediction of the 'transported' ellipse parameters to be made at any other point in the system, by means of a 'sigma' matrix manipulation [5].

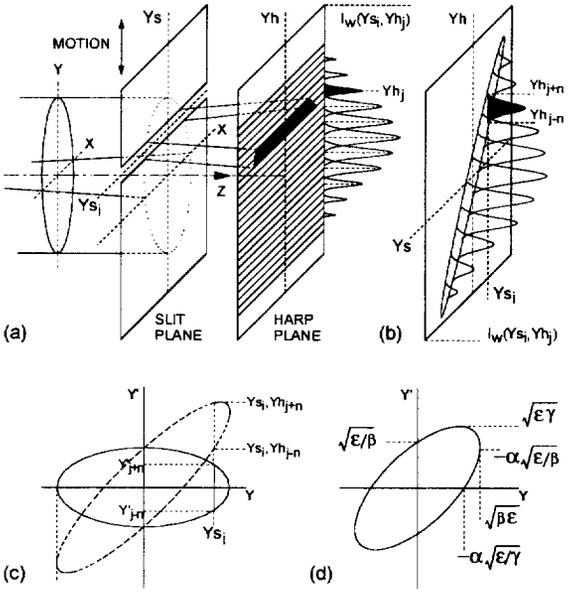

Figure 1. (a) Slit-harp measurement schematic. (b) Beam density distribution in (Ys,Yh) plane. (c) Phase space contour for a gaussian beam with a y-plane waist. (d) Definition of Twiss parameters

A schematic showing the essential features of the slit-harp measurement system is shown in figure 1(a). A beamlet, selected by a moveable slit at Ys_i , is intercepted on a downstream multi-wire detector (harp), as a current density distribution $I_w(Ys_i, Yh_j)$, centred on Yh_j. The profile for each slit position is stored in a two dimensional array, Ys_i, Yh_j. The right ellipse, shown in figure 1(c), represents an rms contour in the Y, Y' plane, for a beam with a gaussian density distribution, and a Y-plane waist. The input data ellipse in the Ys_i, Yh_j plane, shown dotted, indicates how the input data is sheared to generate the Y, Y' phase space data.

3 CONTROL PROGRAM STRUCTURE

Three measurement cycles, beam profile (x, I_{BEAM}, and y, I_{BEAM}), and emittance in the two transverse planes (x,x'), or (y,y'), are initiated and run under program control on an ISIS control system computer.

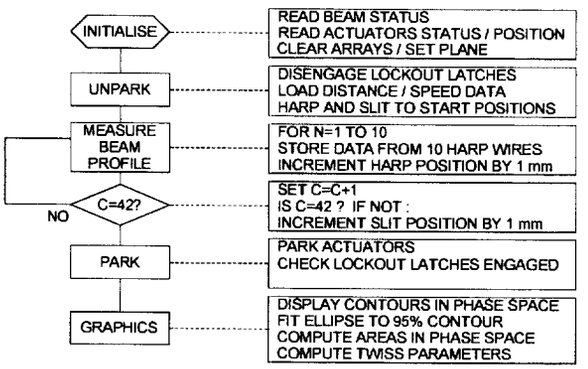

Figure 2: Emittance measurement code structure

The emittance measurement code structure is shown in figure 2. The measurement stores harp data in a two dimensional (42,100) input array, where, for each of 42 x 1 mm slit positions, a beam profile consisting of 100 x 1 mm measurements is made. Input array data is processed (sheared, noise rejected, amplitude normalised), to produce the phase space data array.

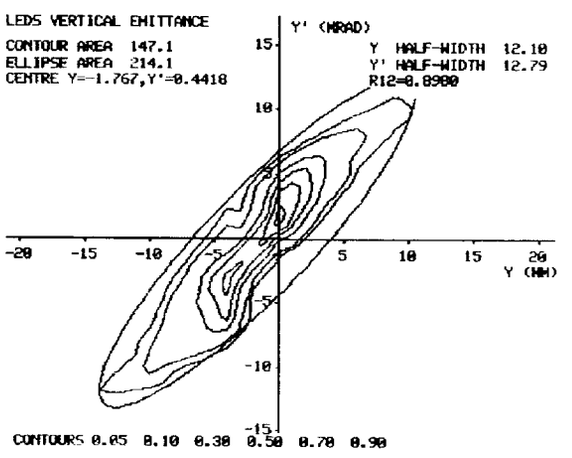

Figure 3: ISIS 665 keV H- Y- plane emittance plot

The phase space data is processed to produce plotting coordinates for a 2D contour map, with contours at 5, 10, 30, 50, 70, and 90% of the normalised peak beam intensity. The area inside the coordinates of the outermost contour is computed, by summing the areas of all the triangles formed by the centroid and successive pairs of contour coordinates. An ellipse is fitted to the coordinates of the outermost contour by first performing a least squares fit, to determine the slope of the major axis, and then, setting the length of the major axis, equal to the maximum width of the contour in the x direction, and the length of the minor axis equal to the maximum width of the contour in the x' direction. Computation of rms emittance is currently performed off-line.

4 MECHANICAL DESIGN

A plan view of the ISIS 665 keV H- beam transport area, showing the location of the emittance measurement installation, is shown in figure 4.

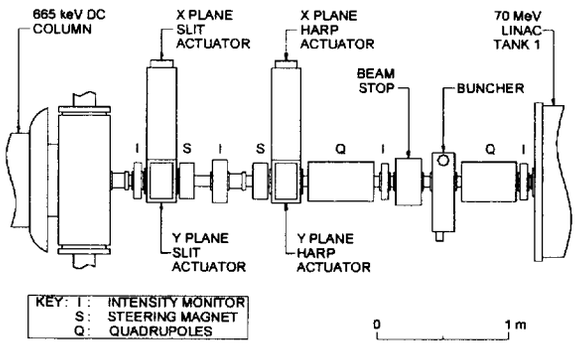

Figure 4: Plan view of ISIS 665 keV H- Beam Transport

The x and y plane harp actuators are located 980 mm downstream from the x and y plane slit actuators. The 1 mm wide, beam analysing slits are formed from copper plate, and are water cooled. ISIS beam prf is reduced from the operational 50, to 50/32 p.p.s. for the measurement duration, resulting in an average beam power of ~ 12 Watts (~ 25 kW peak). The harp assemblies are designed to withstand beam heating during the profile monitoring function at this reduced prf. They consist of ten, 1mm diameter tungsten wires, on a 10 mm pitch, supported by beryllium-copper spring fingers. These are attached to machineable ceramic (macor) blocks, mounted on a stainless steel 'C' frame. The mechanical construction of a linear actuator (y-plane harp) is shown in figure 5. The precision mechanism has a setting accuracy of +/- 1/64 mm. The static load imposed by the vacuum is balanced by an equal and opposite force exerted by a constant tension spring. Reduction of this load has permitted the use of lighter weight, lower inertia components in the drive train. As a typical measurement cycle consists of many small movements, the reduction in drive train inertia, results in a significant reduction in measurement time.

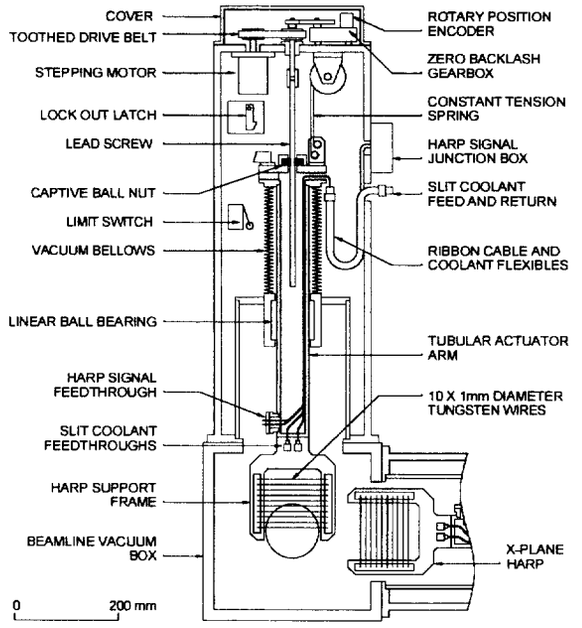

Figure 5: Actuator construction (schematic)

Limit switches prevent actuator movement beyond predefined limits. Lock out latches prevent the possibility of positional 'creep' in the parked position, when the stepping motors, in the de-selected plane, are disconnected from the multiplexed motor drive units.

5 ELECTRONIC DESIGN

The important features of the emittance measuring system drive control, and signal conditioning electronics, are shown in figure 6.

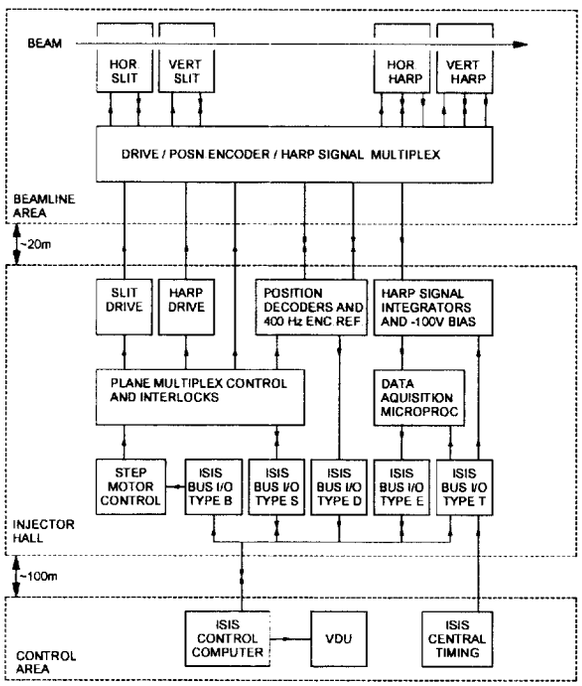

Figure 6: Electronic system schematic

Each linear actuator is powered by a 16 watt, two phase stepping motor [6]. The output of a programmable stepping motor controller, with a pre-set acceleration / deceleration slope [6], is multiplexed via two motor drive units [6], to control the positioning of the pre-selected slit / harp actuator pair. Plane selected slit / harp position measurement signals, derived from rotary, absolute position resolvers, are multiplexed to two resolver to digital decoders with 14 bit output resolution (1 LSB = 1/64 mm). Signals from limit switches and lock-out latches provide status information, and are hard wired to prevent damage under fault conditions.

Harp signal wires are biased at -100 volts, to repel thermionic and secondary electrons, stripped from the H- beam. Signals from the ten harp wires are plane multiplexed to a ten channel gated integrator. Integration time is synchronised to the beam pulse length. Integrated signals are output to the data acquisition microcomputer, where the analogue signals are stored as 12 bit data words, that are subsequently transferred to the control computer under program control.

6 OPERATIONAL EXPERIENCE

A routine measurement of beam alignment in the 665 keV H- transport line, is made after each ISIS ion source change (lifetime ~ 30 days), and normally, a full emittance measurement, taking about 20 minutes, will be made. The profile measurement, enables a more rapid (~30 s) check of beam position and width to be made.

7 ACKNOWLEDGEMENT

Contributions from the following are gratefully acknowledged : S. L. Thomas (ISIS emittance graphics), A. I. Borden , and D. Wright (data acquisition microcomputer and software), ISIS project engineering group (mechanical design), and many others.

REFERENCES

[1] C. Lejeune and K. Aubert, 'Emittance and Brightness', in 'Applied Charged Particle Optics', Ed. by A. Septier, 'Advances in Electronics and Electron Physics, Supp. 13A, 1980, p.159-259.

[2] R. C. Webber, 'Longitudinal Emittance', Proc. of the first Accelerator Instrumentation Workshop, Upton, NY, 1989, AIP Conf. Proc. No.212, p.85-126

[3] O. R. Sander, 'Transverse Emittance', Proc. of the first Accelerator Instrumentation Workshop, Upton, NY, USA,1989, AIP Conf. Proc. No.212, p.127-155.

[4] D. R. Swenson, E. P. MacKerrow, H. C. Bryant, 'Non-invasive diagnostics for H- beams using photodetachment by a focused laser beam', Proc. of the fifth Beam Instrumentation Workshop, Sante Fe, NM, USA,1993, AIP Conf. Proc. No.319, p.343-352

[5] K. L. Brown, B. K. Lear, S. K. Howry, 'Transport .360', Stanford Linear Accelerator Centre Report, SLAC-91 (1977).

[6] Sigma Instruments Inc., Braintree, Mass. USA.

CATHODE MODULATION OF HIGH POWER RF OUTPUT TRIODES OF THE ISIS LINAC

B. Brady, C. W. Planner and A. F. Stevens

Abstract

The Linear Accelerator at Rutherford Appleton Labs has provided particle acceleration for the ISIS Synchrotron since 1984. Solid-state cathode modulators have recently replaced hard-tube tetrodes, previously used for anode modulation of the high power RF triodes. This has afforded a reduction in equipment complexity and volume leading to significant savings both in capital and operating costs. These advantages benefit ISIS by not only improving reliability and availability but allow more economical consideration of the proposed development to increase beam current from 200μA to 300μA [1].

1 INTRODUCTION

The RF excitation for each of the four ISIS Linac cavities is provided by a Thomson TH116 triode operating in grounded grid configuration with pulsed anode modulation. A parallel pair of English Electric CW1600 tetrodes switch the 40kV voltage from a capacitor bank to provide the modulation. The TH116 is self-biased into class AB by a cathode bias resistor. A large platform, isolated to 40kV, houses the CW1600 and associated equipment for modulator operation.

Parasitic oscillation in the series switch tube has, in the past, created severe electromagnetic noise problems, affecting local electronics. These have largely been cured, but occasional problems are still encountered.

Replacement modulator tubes are relatively expensive and this coupled with possible future developments has provided the impetus behind cathode modulation.

On-line development time is severely restricted on operational machines like ISIS. Should new systems prove unsatisfactory, old systems must be easily re-instated. Fast and simple re-configuration is therefore an essential requirement for new systems.

2 ANODE MODULATION

At the time of its design, anode modulation was employed because it was readily available and an established technology. A block diagram of the system at ISIS is shown in Fig. 1. There are several disadvantages with series tube modulation: -

- At the operating current, the modulator tube drops up to 6kV
- Each tube requires a filament supply of 10V at 300A therefore 6kW dissipation.
- 40kV isolation transformer for filament supplies
- 40kV mains isolation transformer for screen and grid supplies also for peripheral equipment
- Fibre-optic link required for grid drive signal
- CW1600 requires anode water cooling and grid/screen air cooling.

In addition, the platform housing the modulator tubes measures approximately 1.8m x 2.1m x 0.9m , giving a volume of 3.4m^3. A photograph of the high voltage platform is shown in Figure 2.

Power consumed by the modulator tube is as follows: -

	kW per tube	kW per system	kW per 4 systems
Filament	3.0	6.0	24.0
Power lost in tubes*	6.0	12.0	48.0
Cooling Fans	-	1.0	4.0
Auxiliaries	1.0	2.0	8.0
Totals	10.5	21.0	**84 kW**

* based on 4kV drop at 120A with 2.5% duty cycle

Currently, the modulator tube replacement rate is around 2.5 per year and costs £20k.

3 CATHODE MODULATION

Cathode modulation allows the full capacitor bank voltage to be used for RF generation. A suitable high value resistor is placed in series with the 3Ω cathode resistor, as shown in Figure 3 and with DC anode volts applied, the TH116 is self biased close to cut off by approximately ~ 40mA. The RF power tube has to dissipate an extra ~ 1kW of power, but this is within the anode power capability of the TH116. For cathode modulation to be feasible, a fast, low impedance, high current switch is required in parallel with the high value resistor.

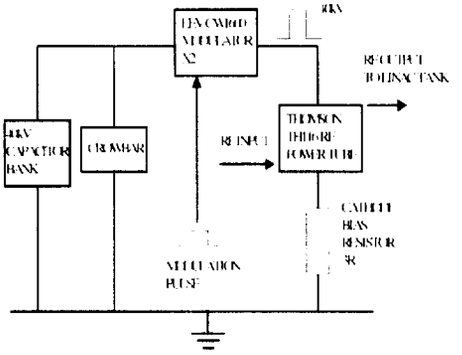

Figure 1. ISIS Linac TH116 Anode Modulation

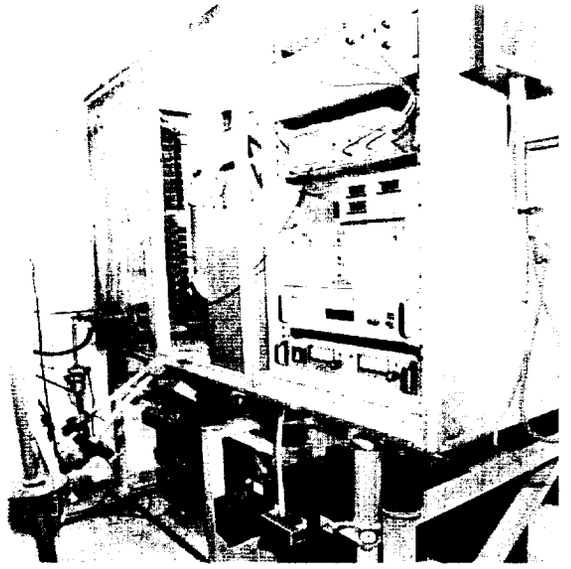

Figure 2. ISIS Linac anode modulator hardware showing the 40kV platform, CW1600 tetrodes, screen and grid power supplies and isolation transformers

3.1 Switching Device Selection

The main criterion for switch selection is based on the ISIS requirements of 200A at a working voltage of less than 800V (the maximum rating of the RF bypass capacitors). Other considerations are complexity, hence reliability, of the device and its drive circuit, conduction and switching losses, availability and cost. A Gate Turn-Off Thyristor (GTO) was considered but the Insulated Gate Bipolar Transistor, (IGBT), has been developed to a point nearer to that of an ideal switch. The problems of 'latch-up' have been eliminated and device ratings have improved considerably. Conduction losses are similar to a GTO, but switching losses are superior. A Semikron IGBT device was selected on the basis of its low inductance package, rectangular safe operating area and constant $V_{CE(sat)}$ levels.

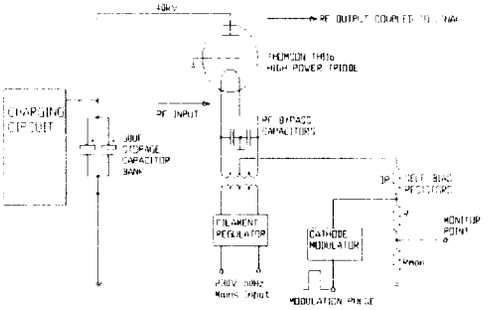

Figure 3. Cathode Modulation Schematic showing the inclusion of a series resistance R for self bias

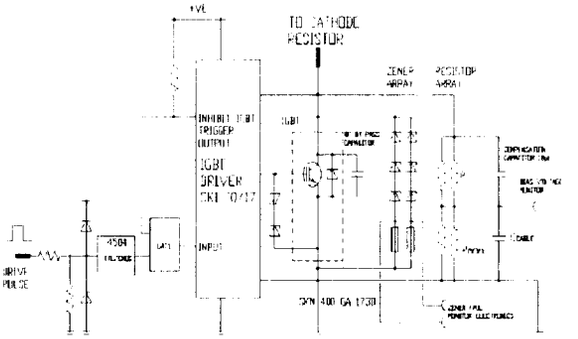

Figure 4. Circuit diagram of cathode modulator

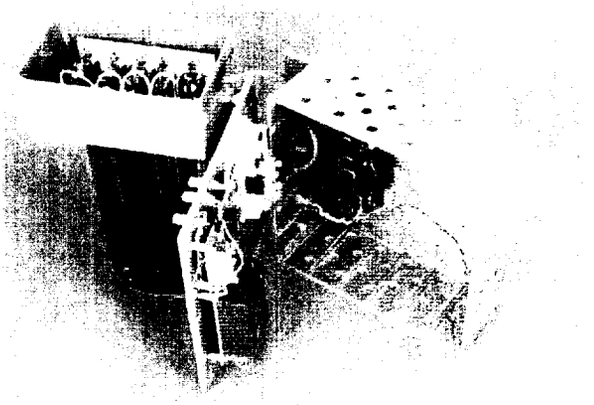

Figure 5. An open view of the prototype cathode modulator indicating the simplicity of the design

3.2 Prototyping

A Westcode WG6016FR12 GTO was used for initial testing, suitable circuitry being developed to achieve reliable switching in the laboratory. However, installed on the TH116 it proved very difficult to switch off the GTO reliably.

A first prototype based on an SKM 200GA 123D IGBT proved very successful and reliable both in the laboratory and when connected in the cathode circuit of the TH116. This unit was installed on the lowest

power linac cavity in December 1997 and ran successfully for several cycles before removal.
A second unit, using a higher power rating IGBT, an SKM 400GA 173D, shown in Fig. 5, was installed on the highest power cavity in March 1998 and is still in operation. A circuit diagram is shown in Figure 4.
Fully engineered versions of the high power unit are under construction and are to be fitted on all four systems later this year.3.3 *Operational Experience*

From early in its development, it was known that the absence of free space loading around the TH116 with dc anode volts > 10–12kV gave rise to parasitic oscillation at ~ 800MHz. The application of RF drive to the tube input, before the modulation of the HT, suppressed this parasite.
Applying RF drive to the TH116 input circuit before modulation is acceptable because the circuit remains a very good RF match. Initial tests using a DC anode voltage established that the parasite did not occur with the tube close to cut-off, but in the cathode modulation switch transition the parasite reappeared. However, parasite suppression in cathode modulation, using pre and post RF input drive results in a large increase in bias, givin
g pulsed voltages across the high value bias resistor before and after modulation, as shown in Figure 6.

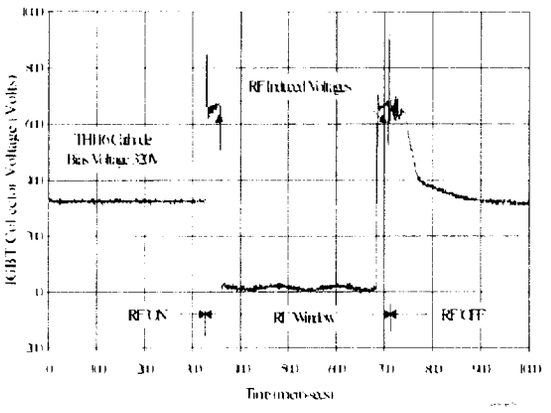

Fig. 6 IGBT collector voltage showing cathode bias voltage at 320V, IGBT switching and RF window.

Calculations on the co-axial RF input circuit of the TH116 shows that 280kW into the 50Ω input transforms to 1.8kV at the grid cathode. The decoupling capacitors are situated at the RF voltage node, but would be destroyed by the increased bias developed by the RF across the large cathode resistor. Transient suppressors were not considered suitable to keep the voltage below 800V because the waveform of double pulses, shown in Figure 6, has a repetition rate of 50Hz. Therefore, a series parallel array of zener diodes was chosen to clamp the maximum bias voltage.

3.4 TH116 Tube Protection

With cathode modulation, protection of the TH116 power tube is required over the whole cycle. Protection
against arc-over is provided by an over current trip triggering a crowbar.
The DC standing bias is also monitored outside the modulation pulse and the tube 'crowbarred' should the bias change by a significant amount. During the modulating time, switching of the IGBT is checked by a built-in slew rate monitor that is used to inhibit triggering of the IGBT.
To maximize operating time, there is considerable built in redundancy. Sufficient resistors are paralleled to form the bias resistor such that failure of one or two resistors does not significantly affect the standing bias. The resistors are run well within their power rating. In the zener array, extra parallel elements are included to allow running should several chains fail. The zeners typically fail short circuit, removal from the circuit is achieved using over current trips with trip indication.

3.5 Radiation

Proximity to possible sources of gamma and thermal neutron radiation made damage to power semiconductors an area of concern. Dosimeter measurements, over one 24-hour period, showed a maximum dose rate of less than 1.7 mSv/hr for gamma radiation and under 0.035 mSv/hr for thermal neutrons. At these radiation levels, lifetimes of several years are expected from the solid state devices.

4 CONCLUSION

Successful operational experience with prototypes on different ISIS Linac tanks has permitted the development of 4 fully engineered cathode modulators. These are to be installed and commissioned within the current long shutdown period.

5 REFERENCES

[1] A Possible Upgrade for ISIS, M R Harold, R G Bendall, T A Broome, I S K Gardner, M G Glover, C R Prior, C W Planner and G H Rees. CLRC RAL. PAC'97, Vancouver, BC, Canada.

UPGRADE OF THE ISIS PRE-INJECTOR EHT GENERATOR

P.J.S.B. Barratt, R.D. Lloyd

Abstract

The thermionic driver stage for the 665kV Cockcroft-Walton EHT generator for the ISIS pre-injector has been replaced with a solid-state 10kVA frequency converter. Control and monitoring are via a Controls Group Standard STEbus microprocessor crate operating under the new ISIS control system based on Alpha workstations running Vsystem. The converter, its associated electronics and control system are described.

1 INTRODUCTION

The -665kV EHT generator for the ISIS pre-injector was supplied by *Emil Haefely & Cie AG* in 1967 and had been in almost continuous use ever since. Although it gave little trouble, its age, and concern about the continued availability of its thermionic tubes and other spares prompted the decision to replace its power electronics with a solid-state 10kVA frequency converter supplied by the U.K. company, *Magnus Power Ltd.*[1]

Its control and monitoring were implemented using an example of the recently-developed Controls Standard STEbus (CSS) [2] embedded microprocessor system which is now being used to interface ISIS accelerator equipment to the Alpha workstations of the new control system via Ethernet.

2 FREQUENCY CONVERTER

Fig. 1 shows the frequency converter as supplied and Fig. 2 shows the controller with its associated STEbus crate. The converter's incoming 400V 3-φ a.c. supply is rectified to 230V dc. This dc supply is fed to three paralleled output Power Modules consisting of four-element bridge circuits, two diagonally-opposite arms of which are switched fully on at any instant, depending on the state of four 56kHz control signals. The mark-space ratio of these control signals determine the output voltage of the Power Modules.

The resonant frequency of the output load on the converter is about 5.5kHz and exhibits some long-term variation. For this reason, the output frequency is programmable from 5 to 6kHz with a resolution of 1Hz. To produce the required output frequency, sinusoidal modulation of the mark-space ratio of the 56kHz control signals is used to produce a sinusoidal output waveform from the Power Modules of up to 120V rms. This voltage is stepped up to 5kV-0-5kV rms, by an external transformer, replicating the push-pull anode outputs of the pentodes of the original Haefely equipment. This output is used to drive the 3400-0-3400 turn primary of the original Haefely transformer. The 66000 turn secondary of this transformer gives the input voltage for the associated five-stage Cockcroft-Walton multiplier to generate the required -665kV.

With full beam intensity, the current required at -665kV is 2.2mA. The actual load on the frequency converter at full beam intensity is 61A at 69V rms giving 4.21kW which can easily be met by only two output Power Modules. Although no failure has yet occurred, a faulty output module could be removed for repairs while allowing continued operation of the converter.

3 CONTROLLER

A block diagram of the controller and STEbus crate is shown in Fig. 3. Four independent dividers monitor the EHT. Their outputs are filtered to remove remanent converter-frequency ripple, sampled to exclude the perturbation in EHT caused by pulses of beam current, and digitised in the ADC. One output is selected for comparison with the EHT demand level from the DAC. The difference error signal is amplified and integrated to set the required output power from the converter. The necessary drive level is monitored as a useful diagnostic of the condition of the rectifiers, etc, of the Cockcroft-Walton multiplier and of the tuning. The reading of the EHT return current to the Cockcroft-Walton multiplier is also digitised. Transient reductions in EHT voltage, caused by voltage breakdowns, are detected for logging.

The controller also provides the usual machine and personnel interlocks.

4 CONTROL SYSTEM AND CSS CRATE

4.1 New ISIS control system

The new control system comprises a network of seven Digital Alpha workstations running the Open VMS operating system and a commercial control system package, Vsystem. Interface to the user is via X-windows multi-window displays (control screens), keyboards, mice and programmable knobs or tracker-balls.

Using the Vsystem [3] Draw package, control screen displays can be generated interactively using a mouse, not only selecting fixed symbols and boxes etc. for display but also linking the screen display through the distributed database to the equipment so as to give continuously updating displays and to allow interactive operator control of equipment.

4.2 CSS Hardware

Interface to the accelerator equipment is via Ethernet to the CSS system employing the IEEE-1000 STEbus standard. It uses *ARCOM CONTROL SYSTEMS Ltd* hardware, driven by software developed in the ISIS Controls Group.

STEbus is an 8-bit bus which uses a master-slave concept in which a master, having gained control of the bus, may address and command slave modules on the bus. The masters and slaves communicate by using an asynchronous interlocked handshake protocol.

With such a system, the speed of data transfer is governed by the slowest participating board, and not by timing figures in the specification. This allows the possibility of performance improvements as and when faster devices become available.

STEbus's protocol does not unduly favour any particular processor family, thereby giving the designer a wide choice of CPUs. The STEbus Control system for the converter uses an *ARCOM* SCIM88-5 CPU card. This forms part of an optimised performance target system based on the Intel 80C188 16MHz microprocessor with 256K bytes static RAM, 256K bytes dynamic RAM and address space of 512K bytes for a FLASH EPROM device (containing the program code). The 80C188 is 100% PC code compatible, which allows code, in our case Borland C, to be developed and compiled on a host PC, downloaded onto the SCIM88 card and then debugged using Arcom's *SourceVIEW* [4], a source-level remote debugger and "ROMing" environment which is powerful and easy to use.

4.3 CSS crate signal processing

A major benefit of the hardware implementation of the *ARCOM* range of Eurocard STEbus cards is the ease with which they can be mixed with other cards made specifically for the application. The signal processing, filtering and sampling of the divider outputs is done on one non-*ARCOM* eurocard and the converter drive level is generated on another. These additional cards do not share the STEbus but are mounted alongside the *ARCOM* cards and are interconnected with ribbon cables.

4.4 EHT Control CSS Software

This software consists of a "round robin" infinite loop which decodes commands arriving from the main control system and actions them via the local application mapping database and equipment and module handlers (hardware access routines).

The Application Software developed for the converter CSS System can be divided into three sections. The first is the local database containing all the necessary software and hardware parameters required to control each channel, the information for which is created by the ISIS Control System and downloaded into the destination STEbus System. The second is the CSS "kernel" which handles the ISIS Ethernet packet protocol decoding; downloading of the database from the Digital workstations; handling of commands to change channel values; update of read values in the database and the calling of various card and equipment handlers required to control the equipment connected to the system. The third is the STEbus I/O card and equipment handlers called by the main control software.

The main control parameters (corresponding to database channels) which are mapped to the application database for the EHT system are as shown in Table 1.

PARAMETER	CARD
Read EHT divider outputs Read EHT current Read converter drive level Set EHT voltage	14-bit ADC/DAC card
Read number of breakdowns Read converter status Reset number of breakdowns Reset converter status	Digital I/O card
Set ADC read time	ISIS Timing card

Table 1: Control Parameters

When the converter CSS control software is not receiving commands, from a Digital workstation, to change one of the above parameters the local control software performs the supervisory role of continuously updating all of the database READ channels and monitoring the Ethernet for incoming data packets. A piece of code called the reader running on a Digital workstation automatically sends a data packet at two second intervals requesting the return of the STEbus system channel values. The values returned are displayed on a Vsystem GUI (control screen).

A command can be sent, for example, to set the EHT via the Vsystem GUI by typing a new value or moving a slider with the mouse. An Ethernet packet is compiled containing, among other things, the new set value, database channel number and destination Ethernet address. The packet is received and decoded by the CSS software and the database channel containing the EHT value updated with the new value. The database channel contains all the necessary information to select the required software handler, via a software switch, to access the EHT demand DAC.

5 COMMISSIONING

In normal operation, there are several EHT breakdowns each day across the pre-injector accelerating column. The resultant transient electromagnetic disturbances have often caused malfunctions of, and even damage to, adjacent electronic equipment. There were initial concerns about the vulnerability of the solid-

state electronics of the STEbus crate, controller and the Power Converter to this interference. The system was therefore installed giving careful consideration to the shielding and routing of cables to minimise the areas of enclosed loops. The converter output transformer, actually positioned in the EHT area, has an effective interwinding screen. Bulkhead co-axial feedthroughs were used for all signal connections through the screen of the EHT area. Transient voltage suppressors and appropriate filtering were used on all system inputs. The system has, at the time of writing, been in continuous use for eight months without damage or significant misbehaviour. The standard deviation of the continuously-monitored EHT voltage is normally less than 100V. The STEbus firmware has required no manual re-initialising despite there being no implementation of a "watchdog" timer facility.

The combination of the new ISIS Controls System, CSS, Arcom's hardware and development software, and an increasing range of card and equipment handlers enables the rapid development of inexpensive, powerful, robust and reliable solutions to SCADA type accelerator controls. The ISIS Controls Group investment in this system is now at least 10 staff-years and the cost of the hardware for a single crate CSS application is typically £2000-3000, depending on the type and number of application cards required.

REFERENCES

[1] Magnus Power Ltd, 29-30 Brunel Rd, St Leonards-on-Sea, East Sussex, TN38 9RT, U.K.

[2] "The Controls Standard STEbus - CSS" Ver 2.0 CLRC 1997. - available from the authors.

[3] http://www.vista-control.com.

[4] Eurocard PC Catalogue. Arcom Controls Systems Ltd, Units 8-10, Clifton Rd, Cambridge, CB1 4WH, U.K.

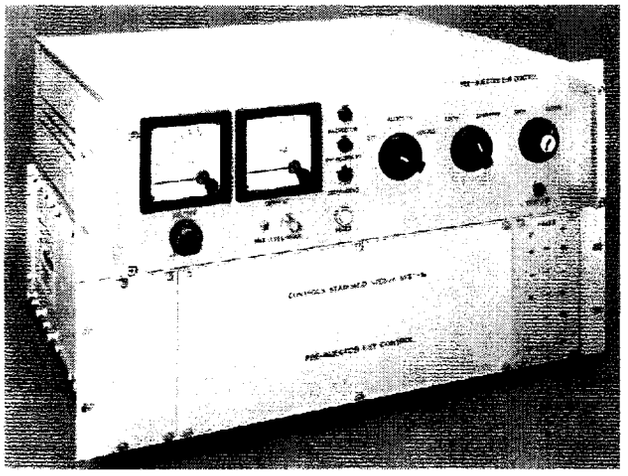

Figure. 2: Controller and STEbus Crate

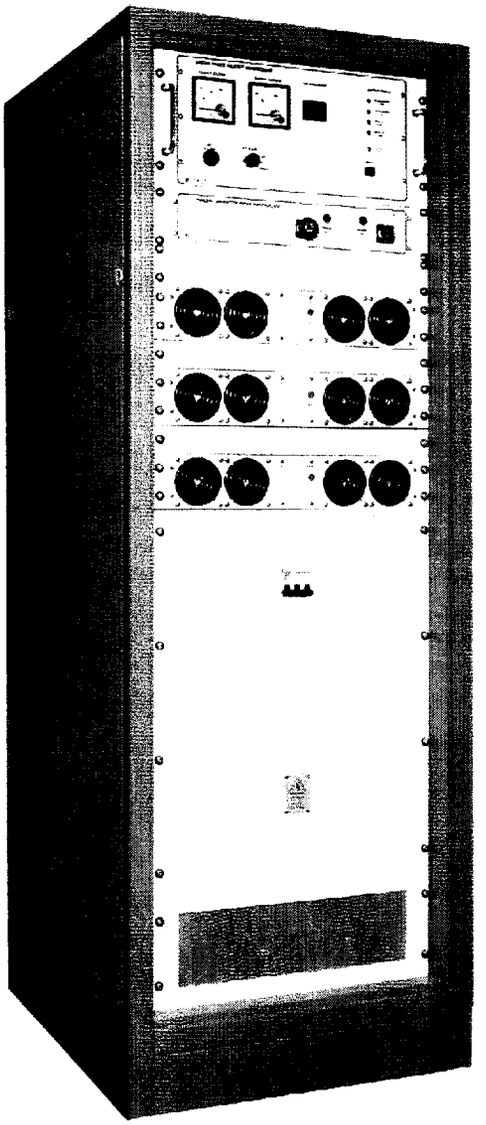

Figure. 1: Frequency Converter

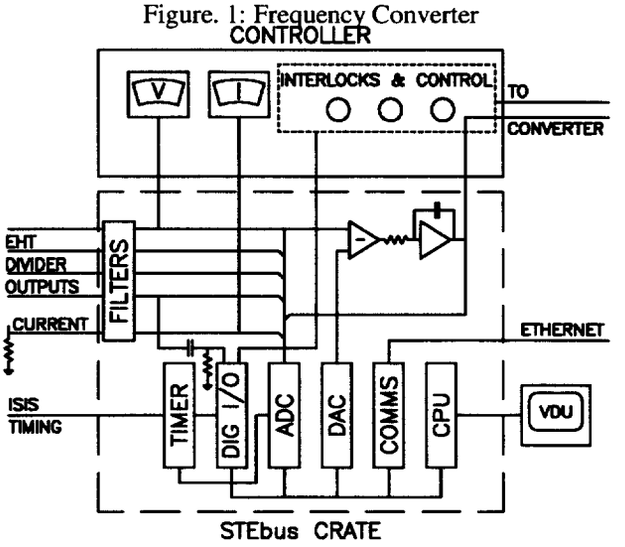

Figure. 3: Block diagram of Controller and CSS crate.

DEVELOPMENT OF THE ISIS SYNCHROTRON DIAGNOSTICS

D.J. Adams, A.I. Borden, A.H. Kershaw, C.M.Warsop, D.M. Wright

Abstract

Developments of the diagnostics system on the 800 MeV High Intensity Proton Synchrotron of ISIS, the Spallation Neutron Source at the Rutherford Appleton Laboratory, are described. Substantial hardware upgrades, including the addition of many fast digitiser channels, improved position monitor amplification, automated signal switching, a DEC Alpha Workstation, improved software for data processing and display, are outlined. The applications of the new system with both normal high intensity beams, and specially configured low intensity 'diagnostic' beams, are also summarised. The new information provided by the system will be a significant aid in set-up and optimisation of the machine.

1 DIAGNOSTICS UPGRADE

1.1 Background and Basic Aims

The ISIS Synchrotron [1] accelerates 2.5×10^{13} protons per pulse at 50 Hz. High intensity beam is established via charge exchange injection over 120 turns. Beam is then bunched and accelerated from 70 to 800 MeV in 10 ms, extracted in a single turn, and transported to the target.

The Synchrotron was built with a comprehensive suite of diagnostic devices, which provide all the information needed to run the machine. However, upgrades to the accelerator control system, and the associated increase in computer power, highlighted the potential for upgrading the diagnostics data acquisition. This upgrade, presently underway, makes fuller use of existing diagnostics, acquiring more detailed information and processing it appropriately. The hardware upgrade is based on the addition of many fast digitiser channels, with software switchable inputs, which can capture most beam derived signals. The dedicated Diagnostics DEC Alpha Workstation, incorporated with the Control System, controls data acquisition, provides power to process and display data, and can control most machine parameters. Automation will promote quick and simple measurements, with high level software providing convenient user interfaces. The increased amount and detail of information will help improve machine control.

1.2 Applications of the Upgrade

The main application for the upgraded system will be acquisition of transverse dynamics information from 20 capacitative position monitors around the ring. The other major application is acquisition of bunch shapes from a capacitative pickup, for studies in the longitudinal plane. Acquiring data from other diagnostics e.g. beam intensity toroids and beam loss monitors, is also planned.

1.3 Low and High Intensity Measurements

The ISIS diagnostics were designed primarily for measurements on high intensity beams, however, these have been complemented recently with the use of specially configured low intensity 'diagnostic' beams [2]. The upgrade will make increased use of these methods. Measurements of low intensity beams, occupying a small fraction of machine acceptances, yield much detailed and accurate information not available from high intensity beams, where interpretation is complicated by averaging and space charge effects. Appropriate diagnostic beams are produced by chopping the normal 200 μs injection pulse to ~100 ns (less than one turn), with an electrostatic kicker. These 'chopped' beams are <1% of normal intensity, which necessitates upgrades to amplification on all position monitors. The low power of chopped beams makes them an ideal 'non-destructive' probe.

1.4 Practicalities

On-line experimentation during operational running is made possible by switching many ring parameters to experimental values for 1 pulse in 128, leaving interleaved 50 Hz pulses unaffected. This is useful for experimentation with high or low intensity beams. In the latter case loss of the experimental pulse has negligible impact on neutron production. Automated experiments, using computer control of machine parameters and data acquisition, will exploit this ability for on-line experimentation.

2 TRANSVERSE MEASUREMENTS

2.1 Basic Method

The new information provided by the system is turn by turn positions at 10 monitors per plane. An example of betatron motion of the beam centroid as observed at a single monitor is shown in Figure 1. Least squares fit analysis [2] of this data provides accurate measurements of Q, betatron amplitude, phase and closed orbits. Data from many monitors on the same pulse are particularly valuable in eliminating pulse to pulse variations and making measurements fast. Most measurements will be possible with either chopped beams or at high intensity.

2.2 Basic Measurements

The turn by turn trajectories have obvious applications for **Q measurement**. High and low intensity

values can be measured using the fast betatron kicker or a steering magnet. Low intensity measurements are particularly useful for ensuring the programmable trim quads are tuning the machine Q's correctly. Automated experiments, measuring Q as a function of each trim quad current, give the beta function at 20 locations and detailed checks on operation of hardware.

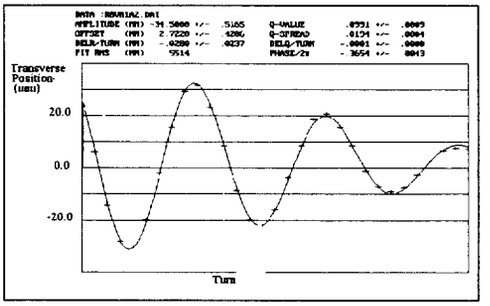

Figure 1: Example of Measured Betatron Motion

The system will allow more comprehensive **closed orbit control**, as well as providing information on turn by turn, and pulse to pulse variations in trajectories. Using automated experiments to scan through currents on all steering magnets, whilst measuring positions at all monitors, gives the 'steering matrices' for correction. Data from these experiments also give lattice information and checks on associated hardware.

Simultaneous measurement of transverse positions of beam centroid at many points around the ring, over ~30 turns, allows measurement of relative beta function at monitors and phase advance between monitors.

2.3 Use of Measurements for Set up

Work reported elsewhere [2] has provided much information on the **injection** process, including direct measurement of 'painting'. However, progress has been limited by the inability to measure closed orbits on AC coupled monitors at injection, when beam is unbunched. Upgraded high gain monitor amplifiers will allow orbit and trajectory measurement with chopped beams. This will give much improved control of injection.

Detailed knowledge of closed orbits and steering matrices will allow thorough **aperture checks** and facilitate the setting up of beam **collectors**, essential for machine protection. Lattice parameters measured all around the ring will improve ability to locate magnet faults and develop lattice models. **Extraction** set up will benefit from orbit control, knowledge of trajectories and improved lattice models.

2.4 Understanding High Intensity Effects

Use of chopped beams to accurately identify best machine set up, perhaps initially optimised empirically at high intensity, will aid systematic optimisation. Complimentary low and high intensity measurements, e.g. Q values, will illuminate high intensity effects. The new system will also allow more detailed studies of fundamental high intensity phenomena, e.g. instabilities.

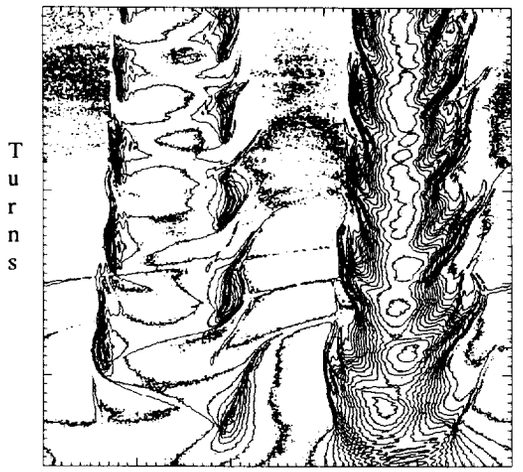

Figure 2: Example of Longitudinal Profile

3 LONGITUDINAL MEASUREMENTS

3.1 Basic Methods

The upgrade allows longitudinal pulse shapes from a monitor to be digitised over thousands of turns at high resolution, quickly providing detailed longitudinal information. Significant computing power is required for processing and display, where development of bunch shapes is calculated as a function of RF phase over many turns. Observation of chopped beams occupying small fractions of RF buckets reveals structure of phase space, e.g. Figure 2, where a bunch is captured unevenly between the two RF buckets.

3.2 Applications

At high intensity, observation of **trapping** and **acceleration** is of considerable interest. The dominant beam loss in the ring is during trapping. This process will now be open to detailed scrutiny, allowing correlation of longitudinal motion with RF loops and data from beam loss monitors. Work is underway to compare measurements with predictions from space charge codes. These studies are important for the proposed dual harmonic RF upgrade to ISIS [3].

4 HARDWARE AND SOFTWARE

The ISIS control system [4] consists of a cluster of DEC Alpha Workstations running the Open VMS operating system. These are connected via ETHERNET to CAMAC, MPX and STE interfaces for hardware control. The controls software is based on the VISTA Controls system, with custom written drivers which link VISTA to the various interfaces. Diagnostics data acquisition hardware and software were chosen to be compatible with these systems.

4.1 Outline of Hardware

The synchrotron ring position monitors each require two digitising channels. **Transverse measurements** use 10 position monitors and therefore require 20 digitising channels. The synchrotron revolution frequency ranges from 0.7-1.6 MHz. Sample rates of 100 MS/s with bandwidths of 100 MHz give the required signal resolution, whilst 250 kbyte record lengths allow 1000's of turns to be acquired. Twenty digitising channels are conveniently supplied using 5, four channel digital storage oscilloscopes (DSO's). **Longitudinal measurements** require data from one monitor digitised at 1 GS/s, with record lengths of ≥1 Mbyte per channel. These are also provided using a DSO. The DSO's are remote controlled using GPIB and include flexible customisable set-ups for beam measurements.

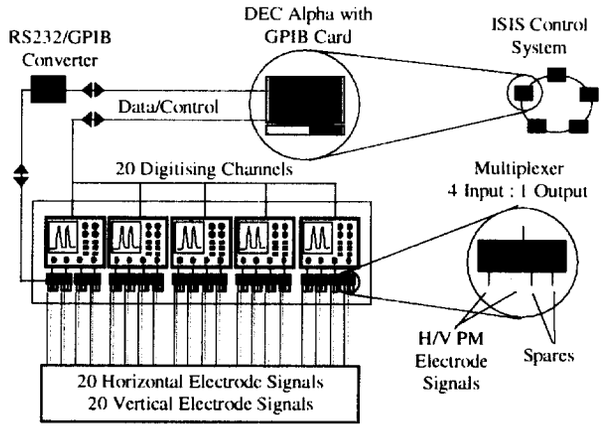

Figure 3 : Schematic of Diagnostics Upgrade

Each position monitor electrode has an amplifier with switchable gain for use with high and low intensity beams. Amplifiers are able to switch between two gain settings within 10 ms, to allow measurement of chopped beams during on-line experimentation.

Signal switching at the input of the digitisers is controlled using twenty, 100 MHz, 1 of 4 way, software controlled switching boxes [5]. These are controlled by GPIB. At present two inputs are used to switch between horizontal and vertical position monitors. Two spare inputs are available for future expansion.

The computer control for these systems is a dedicated DEC Alpha running Open VMS. This provides the necessary processing power for data analysis and display. The workstation is a node member of the cluster and offers full integration with the existing control system over ETHERNET. This allows direct access to synchrotron hardware control. A PCI slot on the DEC Alpha motherboard is used to house a GPIB card. Commercial drivers compatible with FORTRAN provide GPIB card control [6]. Figure 3 outlines the hardware.

4.2 Software

The diagnostics and control software uses two languages, FORTRAN and IDL [7]. Both languages have extensive application libraries and offer calling mechanisms to one another, providing a flexible development environment. Hardware control is driven by FORTRAN application libraries. These have been developed to provide GPIB remote control and data transfer operations for DSO's and switching units. This language is also used for low level calls to the ISIS hardware interfaces for synchrotron control. Graphical user interfaces for measurement control and data visualisation are written in IDL. Data analysis modules called from these interfaces are written in both languages. This choice of software has the additional advantage that it is largely platform independent.

5 STATUS AND CONCLUSIONS

5.1 Status

Most hardware is now installed and development of data processing software and measurements is well underway. Full use of the upgrade is envisaged for detailed beam studies in the years ahead.

5.2 Conclusions

Upgrades to diagnostics data acquisition on the ISIS Synchrotron are making much more detailed information easily available. This will be of great value in running and optimising the machine.

REFERENCES

[1] Spallation Neutron Source, Description of Accelerator & Target, B Boardman, RAL Report, RL-82-006

[2] Low Intensity & Injection Studies on the ISIS Synchrotron, C M Warsop, EPAC 94.

[3] A Possible Upgrade for ISIS, M Harold et al, PAC97

[4] Replacing a Popular Accelerator Control System, R P.Mannix, ICANS XII, RAL Report RAL 94-025

[5] Supplied by Signal Management Ltd., UK.

[6] Supplied by Equicon Software GmbH, Germany

[7] IDL Website: http://www.rsinc.com.

BEAM LOSS COLLECTION ON THE ESS ACCUMULATOR RINGS

C M Warsop

Abstract

The Linac and Accumulator Rings of the European Spallation Source [1] provide a mean beam power of 5 MW, and the need to control beam loss has dominated their design. The function of the beam loss collection system in the two 1.334 GeV accumulators is to localise all loss and associated activation efficiently, in one well shielded region, thereby allowing hands-on maintenance elsewhere. Here, the rings' beam loss collection system is described, detailing the collector system layout and the main parameters optimised, and showing how effective machine protection is ensured under most foreseeable circumstances. Important aspects of the design are: optimising speed and efficiency of halo removal over the ~1000 turns the beam circulates in the ring; minimising halo and out-scatter; heat deposition and activation issues; optimising transverse and longitudinal collector geometries.

1 OUTLINE OF ESS RING COLLECTORS

1.1 Ring Parameters and Design Approach

The two 1.334 GeV rings operate in parallel at 50 Hz. 2.34×10^{14} protons are accumulated in each ring over the ~1000 turn charge exchange injection process; once both rings are filled, beam is extracted in a single turn. The subject of this work is the control of loss once beam has entered the ring.

The design aim has been to optimise primarily for known and likely regular 50 Hz losses, whilst maximising as far as possible protection for irregular or fault loss. The expected regular losses (0.02%) are due to the stripping foil which produces a negative momentum tail and emittance growth. There may also be regular loss due to space charge emittance growth, and irregular losses of all types due to fault conditions. The ring lattice design includes one dedicated long dispersionless straight for collimation. This contains the two main systems: the General Betatron and Momentum Tail Collectors. In addition, there is a General Momentum Collector further downstream, provided for irregular loss.

1.2 Outline Configuration

The **betatron system** is based on the standard configuration of a primary jaw defining the usable aperture, and two secondary jaws for intercepting out-scatter [2], Figure 1. Collimation and full rectangular apertures are 260 and 480 π mm mr respectively. Tolerances indicate optimal betatron phases for secondary collectors are 18° and 163°, but lattice constraints make the latter 140°. Betatron phase advances are roughly equal in the transverse planes, and so jaw assemblies for both are combined in a 'hollow box' construction. The double jawed primaries chosen demand similar secondaries. Double jawed collectors are also included at 90°. Preferred materials are graphite and steel for primaries and secondaries respectively

A special **momentum tail system** was designed into the lattice. Particles losing momentum at the high dispersion injection point undergo enhanced betatron oscillations, these are intercepted at their next maxima 180° downstream in the collector straight. This system is combined with the betatron system; one betatron primary jaw doubles as the momentum tail collector.

The double jawed **general momentum system** is placed at the first dispersion maxima after the collector straight. This will remove low momentum particles leaking from the main collectors, and longitudinal loss.

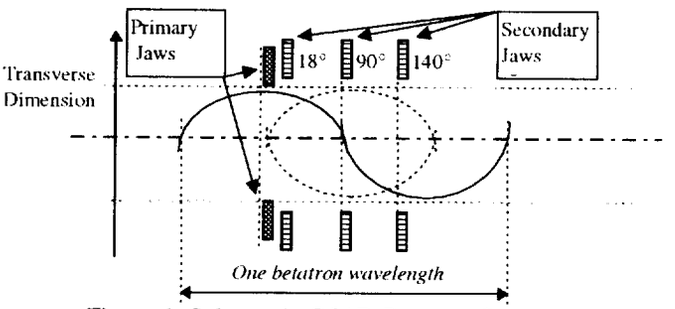

Figure 1: Schematic Of 1D Betatron System

1.3 Key Parameters & Particle Interactions

The basic configuration described leaves many important design choices open, particularly transverse and longitudinal geometry. Basic aims in optimising collector system design are: (i) to minimise out-scatter from the primary collectors, (ii) to minimise or control collection time for halo and (iii) to maximise out-scatter collection. The first two are critically dependent on geometry, the third depends on an optimised set of secondary collectors.

The purpose of the collector system is to localise activation; only particles escaping the shielded collector straight are of interest. These will be mainly protons near 1.334 GeV which out-scatter from the surface of the collector. Most secondary particles (low energy protons, and n, π, μ, e at various energies) will encounter the extensive collimation, which is included in addition to the collector jaws.

For detailed information of *out-scattering protons*, a Monte Carlo code is being developed. However, an approximate physical model is valuable for

understanding and estimating key parameters. Three effects dominate: ionisation energy loss, 'Gaussian' multiple Coulomb scattering and large angle/inelastic nuclear interactions. It is assumed all protons undergoing the last receive enough angular deflection to be removed. This implies exponential attenuation, with 87% removal over 2 mean free paths (λ). Multiple scattering is estimated using a 'Gaussian' spatial distribution [3], calculated at an average energy to allow for energy loss. For graphite, the 1σ beam spatial width is ~5 mm at 1λ (30 cm), increasing rapidly with length. Therefore the probability of out-scatter, Figure 3, is a sensitive function of *impact depth* over ~1 mm scales.

2 TRANSVERSE GEOMETRY

2.1 Model of Collection Process & Simulation

A monochromatic circulating bunch of emittances (ε), can be represented in normalised transverse phase space (X,X',μ) as helically rotating particles on the surface of a cylinder (a.cos(μ(s)+ϕ),a.sin(μ(s)+ϕ),μ(s)), with μ(s) the betatron phase at a point and a=$\sqrt{\varepsilon}$ the amplitude. A short, flat collector at one machine azimuth removes a sector of beam at $\mu(s)=(2\pi Q\ n)$ on the n^{th} turn, Figure 2a. The collection process, defined by parameters such as impact depth and collection time, are non-trivial functions of Q and ε. To study collection of beams with spreads in (Q, ε), in two transverse dimensions, the best approach is a Monte Carlo program.

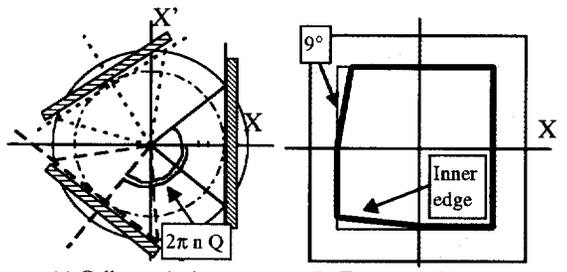

(a) Collector Action (b) Transverse Shape

Figure 2: Collector Action and Shape

Transverse positions for 10^5 particles are calculated at the collector on successive turns with the standard formula, $z_n = A_n \cdot \cos\left[2\pi \cdot Q_z \cdot n + \varphi_z\right]$, until they hit. Uniform random distributions in ϕ [0,2π], and in Q over the expected ranges, are used. Growth rate of the beam *(GR)* is modelled with $A_n=(A_0+GR\ n)$, the betatron amplitude on the n^{th} turn. With this model, the properties of any 2D collector geometry may be assessed as a function of (Q,GR,ε). Most valuable are distributions in impact depth and turns taken to hit. No attempt is made to predict the distributions on the real machine, which are dependent on many unknown parameters. These simulations do however give a detailed knowledge of collector behaviour over all expected 'loss space' (ε, *Q*, *GR*), thus ensuring no 'holes' exist.

2.2 Possible Geometries and Growth Rates

There are two extremes for transverse collector shape: (i) double jawed flat collectors and (ii) single jawed angled collectors, that cover maximum and minimum areas of phase space for a given emittance respectively. The advantage of the first is quick removal of halo. The second collects particles more slowly but generally reduces out-scatter by increasing mean impact depth.

Jaws with angles of 9° relative to the flat are chosen, which give advantages without reducing useful aperture significantly; the inner edge is at $\varepsilon_{inner}=200\ \pi$ mm mr. Growth rates from 10^1-10^3 mm/turn have been modelled. For the normal losses expected typical values are 0-100 μm/turn; values of $\geq$1mm/turn are relatively fast and might be expected under fault conditions.

2.3 Results and Conclusions

Simulations indicate a single angled collector, at typical 1D growth rates, removes 95% of beam in ~10^3 turns at mean impact depths of ~1 mm. Double edged flat collectors remove 95% of beam in ~60 turns, with mean impact depths of ~0.1 mm. Beam circulates in the rings for 10^2-10^3 turns, and it is desirable to remove fast growth within 100 turns. However, tenfold enhancements in impact depths will significantly reduce out-scatter.

Simulations show most desirable properties of both are achieved in a hybrid system with an angled edge at smaller emittances ($\varepsilon_{inner}<\varepsilon<\varepsilon_{coll}$) and additional double flat jaws at the collimator emittance ($\varepsilon\geq\varepsilon_{coll}$), Figure 2b. Quickly growing particles have inherently large impact depths, and are also intercepted efficiently.

3 LONGITUDINAL GEOMETRY

3.1 Length & Scattering on Inner Edge

In order to absorb 1.334 GeV protons and most products, a collector of one proton range (~2m graphite) is required. The main bulk of the collector will for these reasons be one range long. However, the optimal form of the collector edge next to the beam is non trivial.

Consideration of helically rotating particles in transverse phase space, with a collector of significant length, shows particles hit the inner collector edge as well as the front face. Most particles approach the collector at near zero angle, and so hitting the inner edge at zero impact depth enhances out-scatter. In addition, such out-scatter may not be efficiently intercepted, as secondary collectors are optimised for beam emerging near the front face. Calculations show that in a short collector, the front face shadows the inner edge which thus has negligible effect. However, at lengths of over ~4° in betatron phase, this is not the case and significant

out-scatter occurs. Therefore the inner edge at such lengths should be set back with respect to the normalised beam envelope.

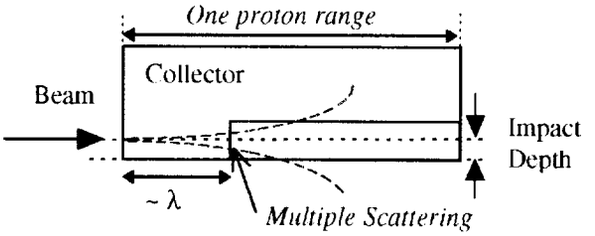

Figure 3: Longitudinal Collector Geometry

3.2 Beam Removal Process & Conclusions

The main removal process in the collector is scattering of the proton or its products into the downstream collector material. The inner face of the primary is a *deflector*. To maximise this scattering the front face should be as many λ as possible, but this increases scattering on the inner edge. Use of a higher A material shortens λ, but disadvantages in increased activation and heat deposition relative to graphite must be considered. The shape presently favoured is flat (normalised) for λ, followed by a set-back of ≈4 mm. This ensures most beam is removed in one turn with minimal interception of the inner edge. A result of the finite length of the inner face is production of protons with significant energy loss, which must be intercepted by downstream collectors.

There are a number of parameters here that need optimisation, and for this more detailed information is required. This will be provided by the 3D Monte Carlo code under development.

4 SECONDARY COLLECTORS

4.1 Essentials & Effect of Primary Shapes

Results from [2] have been applied, and the system has been outlined above. The 90° collectors prevent large emittance particles escaping the system, and allow for isotropic scattering in collector materials. The angled edges of the primary jaws are included on secondaries where practical. Secondary collectors are set at $\varepsilon_{coll+\Delta}$, the collimator limit plus the tolerance set-back, $\Delta \approx 2$ mm.

4.2 Acceptance Allocation

There are three boundaries in the machine acceptance imposed by the collector system ε_{inner}, ε_{coll}, $\varepsilon_{coll+\Delta}$, where primary angled jaws, primary double jaws, and secondary jaws become visible to the beam. At $\varepsilon \geq \varepsilon_{coll+\Delta}$ beam has to pass secondary collectors to escape the system. Projecting all downstream edges back to the primary, Figure 4, shows how effectively the system collimates. In fact few particles with $\varepsilon \geq \varepsilon_{coll+\Delta}$ will escape in one turn, whether resulting from out-scatter or fast fault loss. Therefore, significant protection is provided against very fast growth. Values of these three boundaries may benefit from further optimisation.

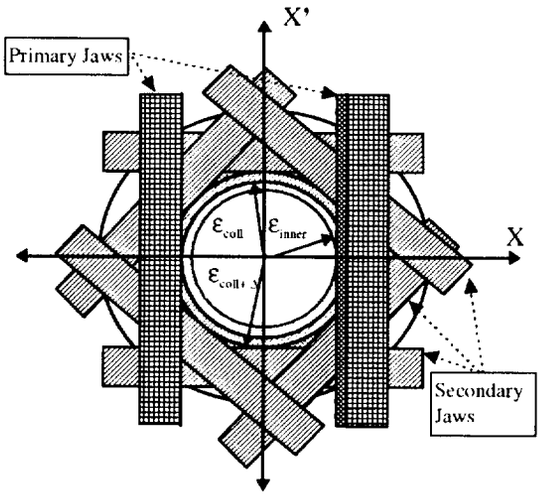

Figure 4: Normalised Phase Space Covered

5 PRACTICALITIES AND CONCLUSIONS

5.1 Construction, Heating and Activation

All collectors will be ~1 m long, modular hollow box constructions, with material extending out transversely ≥5 cm. Usual active handling procedures for quick removal will be employed. Extensive shielding is provided around the collector region. Graphite is preferred for the primary collectors because of its activation properties, and a cheaper steel construction for the secondaries. Heat is spread out over ≥1 m in the low A materials chosen, and the large heat capacity associated with the significant mass of material ensures temperature rises are moderate. Calculations show heating will not be a problem, assuming basic loss protection systems are present. Water cooling is provided for the primary collectors.

5.2 Conclusions

The main parameters of the collector system are established. Studies of the effects of collector geometry, outlined here, coupled with forthcoming Monte Carlo simulation will provide fully optimised designs.

REFERENCES

[1] ESS Feasibility Study, Vol 3, Nov 96, ESS 96-53M, *(available from KFA Julich or RAL).*

[2] T. Trenkler, J B Jeanneret, "Principles of Two Stage Betatron and Momentum Collimation in Circular Accelerators", CERN SL/95-03 (AP), Feb 95.

[3] B. Rossi, "High Energy Particles", Prentice Hall

SIRIUS - A RADIOACTIVE NUCLEAR BEAM FACILITY FOR ISIS

T. A. Broome

Abstract

The design of a Radioactive Nuclear Beam Facility, which could be based on the ISIS accelerator, is described. The facility will use a new 100 μA proton beam, energy 800 MeV directed into a tantalum target. A surface ionisation source followed by mass separation will give beams of radioactive ions at an energy of 200 keV covering a mass range up to 240 amu. Post acceleration to an energy of 10 MeV/nucleon would be achieved using an RFQ and a superconducting linac. Details of the design are described

1 INTRODUCTION

The use of radioactive nuclear beams is an established research tool in a wide range of disciplines including nuclear physics, astrophysics and condensed matter. The success of the existing facilities has resulted in a clear scientific requirement for much higher beam intensities.

A project team from UK Universities and CLRC have carried out a design study for a Radioactive Nuclear Beam Facility, SIRIUS, based on the ISIS 800 MeV, 200 μA proton synchrotron.

The specification was for a facility which could operate at up to 100 μA proton current and deliver high quality radioactive ion beams in the mass range 10 to 240 amu with post acceleration giving up to 10 MeV/nucleon.

At this stage the decision has been taken to base the design on proven technology. Thus a 1^+ ion source has been adopted with the consequence of a more complex post acceleration system than would be required by a multiply charged ion source.

The layout of the proposed facility is shown in figure 1. This was constrained by the topology of the site and the requirement that the SIRIUS facility did not compromise the provision of a second neutron scattering target station at ISIS. There are two experimental areas. One Hall, S4, for the post accelerated beams and the other which will be at a mezzanine level above the linac for three independent beams at 200 keV directly from the ion source. There is space on the site for a further experimental area should this be necessary.

2 EXTRACTED PROTON BEAM LINE

The SIRIUS beam transport line carries a 100 μA, 800 MeV beam from the existing ISIS extracted proton beam line to the new SIRIUS target station. The target station houses two vertically separated targets. The beam line will operate at 16.7 or 25 Hz, depending on whether the ISIS intensity is 300 or 200 μA, and have the capability of switching from one target to the other at 8.3 or 12.5 Hz.

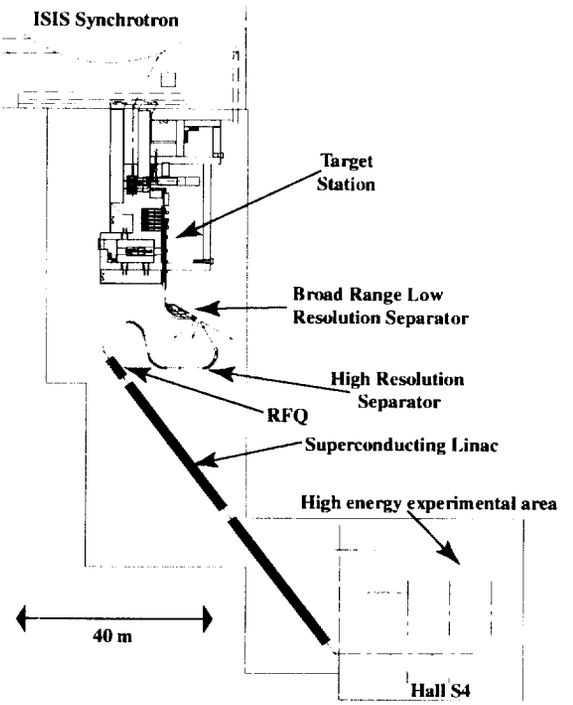

Figure 1 Overall layout of the SIRIUS facility.

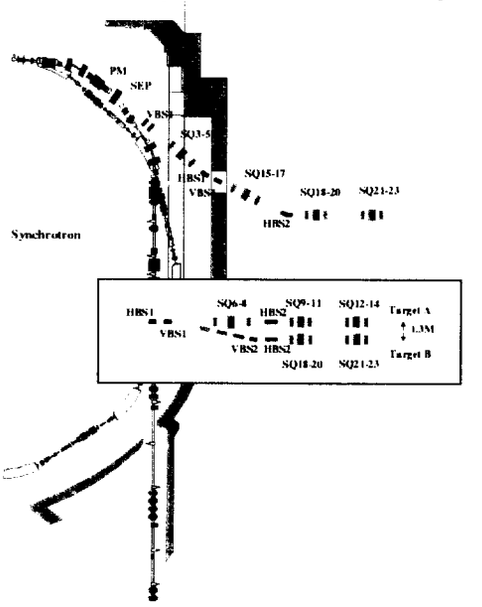

Figure 2 The SIRIUS extracted proton beam.

3 TARGET STATION

The target station has two installed target positions with 1.3 metres vertical separation. These are removed horizontally for servicing or replacement. Figure 3 shows the overall layout. The two target assemblies are at 2.564 metres and 1.264 metres above ground level and each is backed by a separate beam stop. This allows the option of operating each target independently or the operation of both targets simultaneously, if required.

All of the targets and beam stops are contained within a common void vessel that has no inlet proton beam window, therefore the vacuum system in the vessel is the same as that in the extracted beam line. A vacuum valve is installed between the beam line and the void vessel to allow separate pumping of each volume when needed. The two target and two beam stop shielding plugs have circular inflatable all metal seals on their front faces to maintain the beam line vacuum in the void vessel. The void vessel has a removable stepped shielding plug in the top to permit access to the vessel during installation.

The design allows for straightforward replacement of the target/ion source assembly. Servicing takes place in the remote handling cell and complete replacement of the target and ion source in envisaged as a routine operation. This will allow new developments in the technology to be exploited rapidly. Spare assemblies can be condition in the cell or in the storage positions. A change from the operating unit to a conditioned spare will take about 8 hours.

Access into the cooling plant room, target transfer area and remote handling cell is by sliding steel shielding doors and removable roof lintels.

The beam stop behind each target is a cylinder of copper 20 cm. In diameter and 40 cm. long which is edge cooled by a stainless tube wrapped around its length.

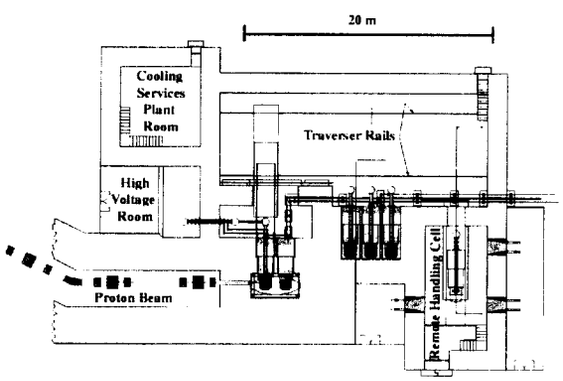

Figure 3 The SIRIUS target station

High voltages are required for both the extraction of the ions from the target and the focus electrode. These are fed through the 3 metre thick shielding plug by a series of concentric aluminium tubes which transmit the voltages, inter-spaced with tubes of insulating aluminium oxide ceramic.

4 TARGET AND ION SOURCE

The initial high intensity targets will be of the RIST design [1], consisting of thin, 25 μm, tantalum foil discs diffusion bonded together to form a rigid assembly and capable of dissipating proton beam powers of ~20-45 kW, at temperatures of 2000-2700 K, by thermal radiation from the finned surface. These targets are 4 cm in diameter and 20 cm long and are suitable for proton beams of 4-7 cm diameter.

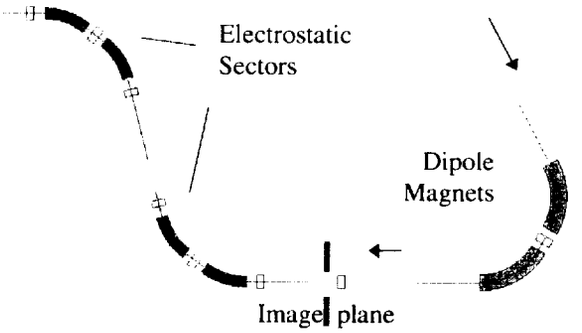

Figure 4 Schematic of the high resolution mass separator based on the ANL [2] design.

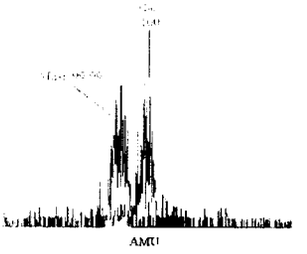

Figure 5 The image at the focal plane of the second magnet for 9999 particles of mass 100, 100.005, and 99.995 amu. The object size is ±0.1 mm and has a divergence of ±20 mr

5 MASS SEPARATORS

5.1 Broad range low resolution mass separator

The separator is designed to deliver four independent beams of different masses simultaneously. The device has a long focal plane simultaneously providing separated beams of mass

5-240. Ray-tracing indicates a minimum dispersion of ~ 6 mm per amu at A=200. This is adequate provided that slits are incorporated in the device in the focal plane where the transmitted beam is to be defined, and that unwanted masses are prevented from painting the contents and walls of the vacuum chamber and its devices.

5.2 High resolution mass separator

A high resolution separator is required to operate at resolutions of $\Delta M/M>10,000$, and as near to 30,000 as possible. to provide mass separation of isobars for the reduction of contamination and for injection into the linac.

To determine the performance of such a separator, illustrated in figure 4, beams with a $M/\Delta M$ of 20,000 have been traced through the magnetic system. A real object of ±0.1 mm and ±20 mr is defocused in the dispersive plane to generate a virtual image of ±0.02 mm and a divergence of 100 mr formed by a quadrupole element prior to the magnet. The entrance and exit faces of the magnets (R=2m) have a small curvature to correct aberations. The virtual image is 2m in front of the first magnet and 1m separtates the two magnets. This drift space can be used for re-focusing or multipole correcting elements. The beam from the first magnet is almost parallel entering the second which focuses 0.427 m down stream, although this can clearly be controlled with quadrupole elements.

The resolution of the system is much better than 1:20,000 as shown in figure 5, and can accommodate an acceptable energy spread in the beam. In the case of a ±5 eV spread in the energy from the ion source, 44% of the central beam is transmitted through an 0.1 mm wide slit at the focal plane, along with approximately 8% of each side mass. This can be decreased by minimising the aberrations in the system.

6 RFQ AND LINAC

The SIRIUS post-accelerator is designed to accelerate radioactive ions initially in a 1^+ charge-state to an energy of 10 MeV per nucleon for a mass range of 10-240 amu. A schematic of the system is shown in figure 6. The ions emerge from the ion-source at an energy of 200 keV. They are matched into the RFQ by setting the RFQ on a high voltage platform to give an injection energy into the RFQ of 1 keV/amu for the entire mass range. The RFQ accelerates the ions to 25 keV/amu from where they are injected into the linac. The linac is combined with foil stripping to give a beam of energy 10 MeV/amu.

Both the RFQ and the cavities are based on designs in use or planned at Argonne National Laboratory [2]. The cavities themselves have been described and costed in reference 3 (a design study for a machine at GANIL). The scheme adopted for SIRIUS is outlined below in figure 6.

The beam from the ion-source is mass separated in the high-resolution spectrometer [see 5.2] before injection into the RFQ section. The RFQ is preceded by a gridded buncher operating at the RFQ frequency (12.125 MHz) which compresses the beam and saves a considerable length of the RFQ normally needed to fulfil this function. The RFQ is just short of 5m in length and accelerates the full range of particles by varying the voltage on the vanes. The device is of the split-coaxial type because of the low frequency. Following the RFQ there is a second gridded buncher and a gas stripper to raise the charge state.

The beam is then injected into a number of super-conducting accelerating cavities. The devices are based on the Argonne frequency of 12.125 MHz and its multiples. The IQWR are described as Inter-digital quarter wave resonators in reference 3. They are essentially combinations of pairs of the two gap quarter wave resonators (QWR) driven by a common RF source.

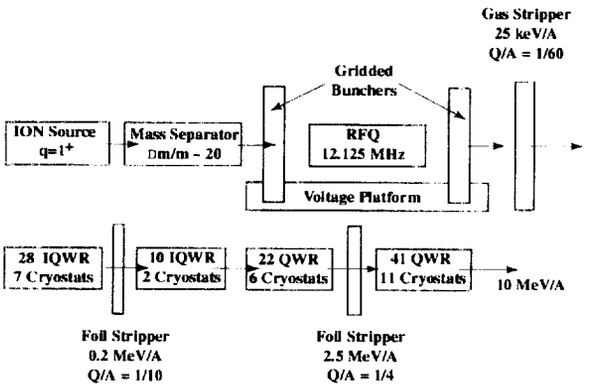

Figure 6 Schematic of post accelerator.

Foil stripping is used at optimal points along the linac to raise the charge state and to improve the accelerating efficiency. As the beta of the beam increases, a switch is made to the individual QWR since the structure is becoming larger and more use can be made of the accelerating field by independent phasing.

REFERENCES

[1] J.R.J. Bennett, C.V. Densham, P.V. Drumm, W.R. Evans, M. Holding, G.R. Murdoch and V. Panteleev, Nucl. Instr.and Meth. B, **126**, 117 (1997).

[2] "Concept for an advanced Exotic beams facility Based on Atlas", 1995.

[3] "Proposition d'un ensemble de production et d'acceleration d'ions secondaires a GANIL", GANIL R 92 04.

A SINGLE PULSE METHOD FOR MEASURING THE RELEASE CURVES OF RADIOACTIVE NUCLEAR BEAM TARGETS

J. R. J. Bennett

Abstract

A simple technique for measuring the release curves of radioactive nuclear beams produced by the impact of high energy protons on thick targets is described. It should allow the data for a complete release curve to be collected from the decay of the radioactive beam produced by one short pulse of protons on the target. The method should provide data more quickly than the conventional one, where individual points on the curve are taken in separate proton pulses at time intervals of several seconds or longer. Moreover, the accuracy should be at least as good, if not better in many cases.

1 INTRODUCTION

The time dependant release of radioactive ions from a hot target, bombarded with high energy protons, and followed by a suitable ioniser, generally fit a characteristic release curve [1]. A short pulse of protons on the target gives a current of radioactive ions which initially rises from zero to a peak and then falls, as shown in Figure 1 (typical result for ^{8}Li from a RIST [2,3] tantalum foil target measured at ISOLDE [4]). This release curve can be used to give an indication of the properties of the target and its suitability for the production of rare short lived isotopes. Also, it is hoped that the curve can be used to help in the design of better targets through an understanding of the fundamental process occurring in the target such as diffusion and effusion.

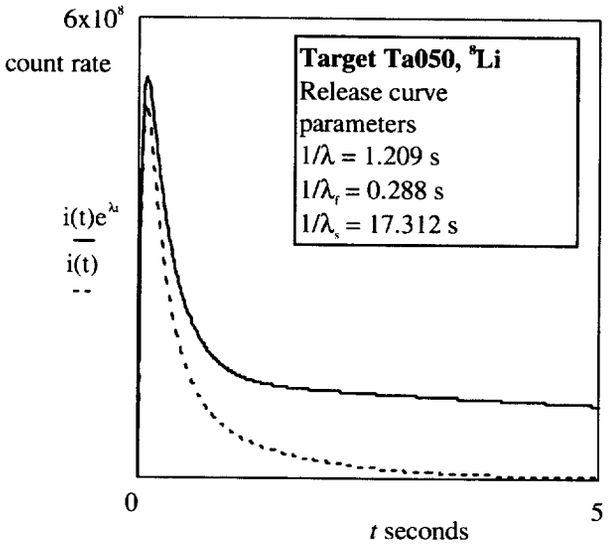

Figure 1. Release curves $i(t)$ with and without decay.

Measurements [1,3] of the release curves from radioactive beam targets have been taken at ISOLDE by putting a single pulse of protons onto the target, transporting a time gated portion of the beam to a tape station and counting the beta decay particles. The number of beta counts, $n(t)$, is plotted as a function of the time delay, t, of the gated radioactive beam, measured from the arrival of the proton pulse on target (t = 0). The measurements are repeated at different delay times to build up a complete release curve

This note considers a different way of measuring the release curves, using all the information in the release from a single proton pulse, and compares the two methods.

2 THE TAPE STATION MEASUREMENTS

Several methods [1,5] of measuring the release function have been reported to have been used at ISOLDE. The tape station system, shown schematically in Figure 2, counting beta decays using a ~4π detector of scintillators surrounding the tape and photomultipliers, will be described here.

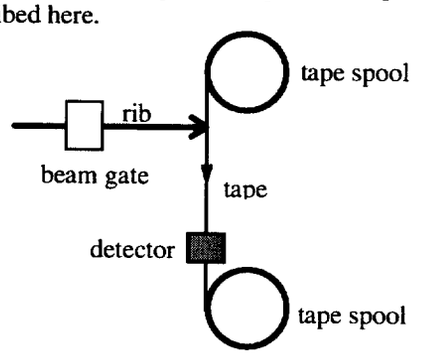

Figure 2: Schematic diagram of the tape station.

Assume that the proton beam hits the target in a short pulse at time zero. The radioactive beam produced by only this pulse of protons is gated to allow a pulse, of length t_c, (the collection time) at time t, to arrive at the tape station and this is deposited on the tape. The tape is then moved over a time t_t so that the radioactive deposit is inside the beta detector array. Then the beta decays are counted for a time t_m, (the measuring time). The detector count $n(t)$ is proportional to the current of radioactive particles that hit the tape at time t in the collection time, t_c. The radioactive beam current on the tape is,

$$i(t) = C\frac{n(t)}{t_c} \qquad (1)$$

If t_c is long, so that the decay or the release function cause appreciably changes to $i(t)$ during the collection, then corrections must be made. Corrections must also be made for the efficiency of the beam transport system from ion source to the tape, the efficiency of the detector and the radioactive decays before the particles reach the tape measuring position. The detector may not only count betas, but also gammas etc. from the decays. Daughter decays and background may need to be considered. The constant C in the above equation takes account of all the corrections.

Repeating the measurement, with the beam gate opening at different times and the tape moved to a new start position, allows a release curve to be plotted.

3 THE RELEASE CURVE

An empirical formula can be fitted to the release curve measurements of the form,

$$p(t) = A\left(1-e^{-\lambda_r t}\right)\left[Be^{-\lambda_f t} + (1-B)e^{-\lambda_s t}\right] \qquad (2)$$

where $p(t)$ is the probability of release of an particle, $1/\lambda_r$, $1/\lambda_f$ and $1/\lambda_s$ are the rise, fast fall and slow fall time constants respectively and A and B are constants. This formulation fits the data very well in most cases. By definition, the integral of $p(t)$, from 0 to ∞, is 1 and the constant A is given by,

$$\frac{1}{A} = \frac{B}{\lambda_f} + \frac{(1-B)}{\lambda_s} - \frac{B}{\lambda_f+\lambda_r} - \frac{(1-B)}{\lambda_s+\lambda_r} \qquad (3)$$

The actual current of particles measured is,

$$i(t) = c \cdot p(t)e^{-\lambda t} \qquad (4)$$

where c is a number to convert from probability to current and the exponential term, $e^{-\lambda t}$, takes into account the radioactive decay of the particles, time constant $1/\lambda$.

4 THE SINGLE PULSE METHOD

In principle, it is possible to measure the release curve in a single pulse by observing the current of radioactive ions directly. The radioactive decay would be a problem if it caused a change in the recorded current, as would be the case for beta decay used in the usual tape measurement system. An alternative is to implant the radioactive beam current from a single proton pulse onto the tape and then measure only the beta decays in a scintillator at the back of the tape. About half the decays would not be measured because the solid angle presented by the scintillator to the tape can not exceed 2π. The electronics could be made to measure the count rate and/or the integrated count (the yield). Figure 3 shows the system schematically.

The measured counts are the result of the decays from the radioactive beam pulse on the tape. In an element of time, ΔT, at time T, the number of particles hitting the tape is $n(T)\Delta T$. The particles have a decay rate of λ. At some time t, later than T, the decay rate of these particles is,

$$D(t) = c \cdot p(T)e^{-\lambda t}\lambda\Delta T. \qquad (5)$$

Integrating over time T from 0 to t, gives the resultant decay rate at time t of all the elements ΔT up to time t,

$$D(t) = c\lambda e^{-\lambda t}\int_0^t p(T)dT. \qquad (6)$$

$$D(t) = c\lambda e^{-\lambda t}A\left\{\begin{array}{l} B\left[\dfrac{\left(e^{-lt}-1\right)}{l} - \dfrac{\left(e^{-\lambda_f t}-1\right)}{\lambda_f}\right] \\ +(1-B)\left[\dfrac{\left(e^{-mt}-1\right)}{m} - \dfrac{\left(e^{-\lambda_s t}-1\right)}{\lambda_s}\right] \end{array}\right\} \qquad (7)$$

where $l = \lambda_r + \lambda_f$, and $m = \lambda_r + \lambda_s$. This decay rate and the usual tape measurement $i(t)$, for comparison, are shown in Figure 4. It will be seen that the peak of the decay curve is 5 times smaller than that of the current, $i(t)$, and delayed by about 1 second - the decay time constant for ^{8}Li.

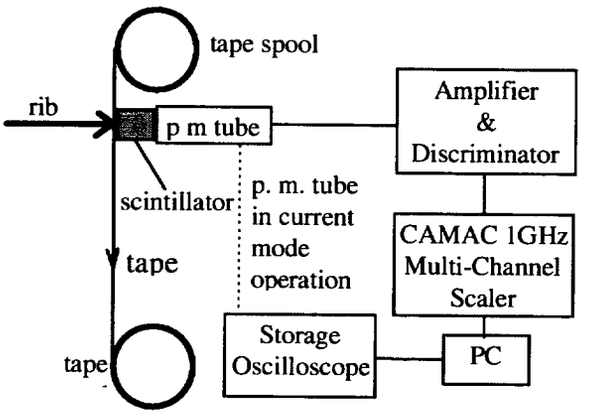

Figure 3: Schematic diagram of the tape station and counting system for the single pulse method.

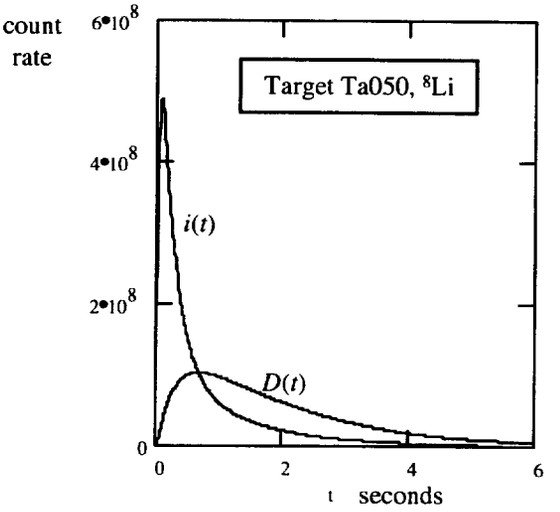

Figure 4: Decay rate $D(t)$, single pulse method. Also, shown for comparison is the current $i(t)$ taken by the conventional ISOLDE method.

Thus by measuring the decay rate of radioactive ions implanted in the tape (produced by a single pulse of protons on the target), it is possible to find directly the parameters of the release curve (2) by fitting the curve (7) to the measurements. It is unnecessary to differentiate the measured curve to reform it into the normal release curve.

5 MEASUREMENT RATE

In the conventional tape measurement, a large number of decays are counted over a long period of time from a small sample of radioactive beam deposited on the tape in a short time and then transported to the counting station. The total count for ^{8}Li is typically up to $4x10^{4}$ in several seconds, a rate of ~10 kHz. However, much higher count rates are required in the single pulse method. The maximum count rate may be limited by the response of the scintillator, the photomultiplier tube and the electronics. Plastic scintillators can be obtained which give a pulse length of less than 10 ns. Photomultipliers can count at rates over 100 MHz. Electronics are capable of very high count rates, up to 1GHz, into bins of less than 1 μs. Discriminators are limited to about 300 MHz. Overall, system count rates of up to 100 MHz are probably feasible.

Reference to Figure 4 shows that rates of 100 MHz are required. However, the scintillator can only enclose 2π of the tape solid angle and it is assumed that the count rate is halved. So the true count rate for $N(t)$ is ~50 MHz, which is just a little high if pulse pile up is to be avoided. By making the scintillator accept a smaller solid angle the count rate can be reduced for measurements around the peak of the curve.

Alternatively, instead of counting the individual particles, the current flow can be measured by the voltage induced across a dynode of the photomultiplier. This can be displayed and measured directly on a digital oscilloscope and is capable of very high effective count rates, $\sim 10^{10}$. In this case the error due to the number of particles counted is very small. At lower radioactive decay rates, the measurements can revert to counting individual decays.

6 ACCURACY

The accuracy of the measurement is basically due to the statistics of the count. The fractional error in N counts is $N^{-½}$. If the collection time is 4 ms (typical of the example of ^{8}Li shown here) the number of counts measured in a point will be up to $\sim 10^{6}$ for the normal ISOLDE method, while in the same time interval it is only $\sim 2x10^{5}$ counts (maximum) with the single pulse method. The fractional error in the counts is less than 10% over a range of times from ~0-10 s and ~0-12 s in the two cases respectively.

Typically there will be up to ~40 points measured using the ISOLDE method for practical reasons of limited time, but the measurements are semi-continuous in the single pulse method - for example, with the counting bins set to 4 ms, there will be 250 points measured per second. It can be shown that this significantly improves the accuracy of calculating the parameters of the release curve from the single pulse measurements. In essence all the data from the release is being used in the single pulse method as opposed to the data only being used from selected small time intervals with the conventional ISOLDE method.

Also, with the single pulse method, it is relatively easy to repeat the complete measurement several times to improve the accuracy, or to rapidly obtain another set of parameters as target/ion source conditions change.

7 CONCLUSIONS

It is possible to make a measurement of the release curve in a single pulse release from the target to a greater accuracy than the conventional method used at ISOLDE with a limited number of measurements. It is particularly useful in providing release curve parameters where any of the time constants are fast, and in particular for fast rise times and short decay times. The method gives an advantage in terms of speed of measurement, looking at slow transients in the target or ion source and the possibility of repeating the measurement many times.

Also, the yield is obtained directly by integrating the total counts obtained in a single proton pulse. The yield is an important parameter since it is the ultimate measure of the speed and success of a target/ion source.

ACKNOWLEDGEMENT

Helpful discussions with Paul Drumm are gratefully acknowledged.

REFERENCES

[1] J. Lettry, R. Cathrall, P. Drumm, P. van Duppen, A.H.M. Evenson, G.J. Focker, A. Jokin, O.C. Jonsson, E. Kugler, H.L. Ravn, ISOLDE Collaboration, Nucl. Instr. and Meth. B **126**, 130, (1997).

[2] J.R.J. Bennett et al., Proc. 5th European Particle Accelerator Conf., Barcelona 1996 (IOP, Bristol, 1996).

[3] P.V. Drumm et al., Nucl. Instr. and Meth. B **126**, 121, (1997).

[4] E. Kugler, D. Fiander, B. Jonson, H. Haas,A. Prewloka, H.L. Ravn, D.J. Simon and K. Zimmer, Nucl. Instr. and Meth. B **70**, 41, (1992).

[5] J. Lettry, R. Cathrall, G. Cyvoct, P. Drumm, A.H.M. Evenson, M. Lindros, O.C. Jonsson, E. Kugler, J. Obert, J. C. Putaux, J. Sauvage, K. Schindl, H.L. Ravn, E. Wildner, Nucl. Instr. and Meth. B **126**, 170, (1997).